Calculation of Garnet Fractionation in Metamorphic Rocks, with Application to a Flat-Top, Y-rich Garnet Population from the Ruhla Crystalline Complex, Central Germany

A. ZEH*

MINERALOGISCHES INSTITUT DER UNIVERSITÄT WÜRZBURG, AM HUBLAND, D-97074 WÜRZBURG, GERMANY

A mathematical approach is presented for the calculation of the major and trace element fractionation that is caused by growth of zoned garnet in metamorphic rocks. This approach is based on textural and compositional parameters directly obtained from natural examples. It takes into account the mode and composition of all unzoned minerals, as well as the mode, crystal size distribution and zonation patterns of garnet grains of different sizes within a certain rock volume. These parameters can be used to fit functions from which the amount of garnet fractionation at each step of a garnet growth history can be calculated. The approach is tested for two compositionally distinct domains within a single garnet–biotite gneiss sample from the Ruhla Crystalline Complex. This sample contains unusual flat-top garnet grains with Y_2O_3-rich cores. It is shown that MnO, FeO and Y_2O_3 are extremely fractionated during garnet growth, but in different ways, and that MnO fractionation does not obey a Rayleigh function. To demonstrate the influence of garnet fractionation on P–T path estimates, quantitative phase diagrams in the model system Na_2O–K_2O–CaO–MnO–FeO–MgO–Al_2O_3–TiO_2–SiO_2–H_2O are constructed by means of the computer software THERMOCALC. The good agreement between calculated and observed mineral assemblages and garnet compositions for all fractionation steps indicates that the new approach can be used to infer detailed P–T paths, even for rocks that contain complexly zoned garnet grains. The results indicate that garnet growth in the metapelite under investigation occurred along a linear P–T path from 470°C and 2·7 kbar to 580°C and 8·5 kbar. The results also show that garnet cores with high Y_2O_3 contents of about 1 wt % nucleated over a temperature interval of c. 90°C, indicating that Y in garnet is relatively insensitive to temperature changes.

KEY WORDS: *garnet; fractionation; pseudosection; yttrium; THERMOCALC*

INTRODUCTION

For petrologists it is a well-known problem that the effective bulk-rock composition changes during the growth of zoned garnet porphyroblasts, and that this effect may have an important influence on the inference of detailed *P–T* paths from metamorphic rocks (e.g. Spear *et al.*, 1990; Stüwe, 1997; Vance & Mahar, 1998; Evans, 2004; Konrad-Schmolke *et al.*, 2005). This problem can become particularly acute when *P–T* paths are inferred from garnet isopleth thermobarometry using quantitative phase diagrams (*P–T* pseudosections). Such diagrams are commonly constructed for a fixed bulk composition, neglecting the successive change of the effective bulk composition caused by element fractionation as a result of zoned garnet porphyroblast growth (e.g. Powell *et al.*, 1998; White *et al.*, 2000, 2001; Zeh, 2001; Zeh & Holness, 2003). Several questions arise in this context: How does the effective bulk composition

*Telephone: +49-931-8885415. E-mail: armin.zeh@mail. uni-wuerzberg.de

change if a fractionating phase such as garnet is formed along a certain P–T path? What are the consequences of this change for the topology of a phase diagram and related garnet isopleths? Has this change any influence on the form of an inferred P–T path and, thus, on the eventual geotectonic interpretation?

To quantify the change of the effective bulk composition caused by zoned garnet growth in metamorphic rocks, four methods have previously been applied. The first method was introduced by Spear et al. (1990), who calculated the change of the effective bulk-rock composition by forward modelling of porphyroblast garnet growth along a certain P–T path using the GIBBS method. This method, however, only permits the calculation of the fractionation effect on theoretical mineral assemblages in thermodynamic equilibrium.

Marmo et al. (2002) proposed an alternative approach, i.e. quantitative compositional mapping of an entire thin-section, to make estimates of fractionation volumes by geometric extrapolation from a two-dimensional section to a three-dimensional volume. The main uncertainties with this method result from the extrapolation procedure, which must account for the effect of cutting zoned garnet porphyroblasts.

A third method was introduced by Evans (2004), who used the lithogeochemical analysis of a metapelitic rock sample of 1·5 kg weight and the measured MnO, FeO, MgO, CaO, and Al_2O_3 contents of a few garnet grains. The effect of garnet fractionation was calculated by applying a Rayleigh fractionation model for MnO in garnet (Hollister, 1966) in conjunction with composition vs modal proportion curves. As demonstrated by Evans (2004), this method, in combination with the application of the computer software THERMOCALC (Holland & Powell, 1998), allows the simultaneous consideration of microstructural, P–T, and chemical evolution of metapelitic rocks during garnet growth. However, as stated by Evans (2004), an essential prerequisite to use a Rayleigh fractionation model is that the manganese growth zonation of garnet is not controlled by kinetic factors and/or altered by diffusion. Nevertheless, chemical fractionation during garnet growth cannot in every case be envisaged as a Rayleigh fractionation process, as demonstrated by Hirsch et al. (2003), Konrad-Schmolke et al. (2005) and in this study. Furthermore, Evans' method requires that all garnet grains in a certain rock volume show the same zonation patterns and that the rims of all garnet grains are in equilibrium at each point during garnet growth. For kinetic reasons such equilibrium conditions may, however, not be maintained throughout the entire garnet growth history (e.g. Chernoff & Carlson, 1997). Furthermore, the rock volume used for the lithogeochemical analysis must be representative of the rock volume from which the garnet zonation profiles are obtained (thin section or part of it).

A fourth method has been described by Konrad-Schmolke et al. (2005), who performed theoretical garnet fractionation calculations along a given P–T path in a metabasic rock with an average mid-ocean ridge basalt (MORB) composition using the computer software THERIAK-DOMINO of de Capitani & Brown (1986), which is based on a GIBBS minimization approach. Konrad-Schmolke et al. (2005) presented different theoretical models that should allow the petrologist to predict different garnet zonation patterns in metabasic rock, depending on mineral assemblage, bulk-rock fractionation, and various kinetic effects.

In this study a new approach is presented, which allows the calculation of garnet fractionation effects in nearly all kinds of metamorphic rocks. In contrast to previous studies, this approach is strictly based on careful textural and chemical analyses of all minerals within a certain rock volume, e.g. within a thick section or a part of it. The input parameters used for the fractionation calculations are the mode and compositions of all zoned and unzoned minerals observed within a certain rock volume. In addition, the crystal size distribution (CSD) of the garnet population and the zonation profiles of garnet grains of different sizes are considered. It will be demonstrated that this textural and compositional information can be used to fit a number of mathematical functions for the precise calculation of element fractionation at different garnet growth steps within a restricted rock domain. It will also be shown that the new method can be used to calculate both major and trace element fractionation during garnet growth. Finally, the influence of garnet fractionation on phase diagram topologies, garnet isopleths and P–T vectors is tested by constructing quantitative phase diagrams in the model system Na_2O–K_2O–CaO–MnO–FeO–MgO–Al_2O_3–TiO_2–SiO_2–H_2O (NKCMnFMATiSH) for different fractionation steps using the computer software THERMOCALC (Holland & Powell, 1998).

PETROGRAPHY
The studied example

The investigated garnet–biotite gneiss sample was collected from the Ruhla Group, which forms the westernmost unit of the Ruhla Crystalline Complex (Fig. 1). A detailed description of the geology of the Ruhla Crystalline Complex has been given by Zeh (1996). The sample location is near the summit of the Breitenberg, situated NE of the town Ruhla (German map coordinate system: HW:5640760, RW:3596990). The sample was taken from the centre of a c. 5 m^2 gneiss outcrop, which shows a steeply dipping foliation (S_1). The S_1 foliation is traced by biotite–garnet-rich layers, which alternate with plagioclase–garnet-rich layers on a millimetre scale (Fig. 2). Locally, the gneissic fabric is
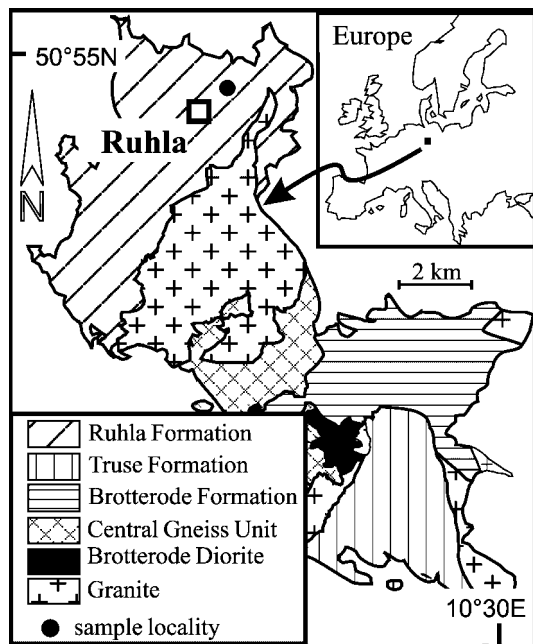
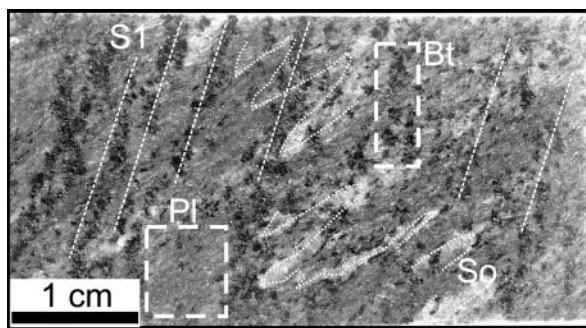**Fig. 1.** Geological map of the Ruhla Crystalline Complex.

Fig. 2. Thin section, showing the location of the investigated plagioclase-domain (Pl) and biotite-domain (Bt). So, isoclinally folded quartz layers; S1, foliation.

transected by isoclinally folded quartz-rich layers, and contains angular, plagioclase-rich but nearly biotite-free domains of c. 1 cm^2 (Fig. 2). Toward the margin of the gneiss body, the S_1 foliation is progressively transected by a younger, flat-lying foliation (S_2), which leads to the transition to a phyllonitic schist.

For the purpose of this study, modes, compositions, zonations and CSDs of garnet grains were investigated in a plagioclase-rich domain of about 15·5 mm^3 (P-domain) and in a biotite-rich domain of about 11·3 mm^3 (B-domain) of a thick section with an original thickness of 518 μm and 20 mm × 30 mm size (Fig. 2, Appendix A). In addition, the mode and composition of all rock-forming minerals in the two domains were analysed using a thin section, which remained after grinding the original thick section to a thickness of

Table I: Results of point counting analyses and thick-section garnet CSD investigations

	P-domain	B-domain
Mineral mode (vol. %)		
Number of counted points	554	532
Grt	12·2	11·1
Bt	6·9	23·3
Pl	62·5	29·5
Qtz	15·5	35·2
Chl	1·3	0·4
Ms	0·4	<0·1
Ru	0·9	0·4
Ap	0·2	0·2
Sum	100·0	100·0
CSD investigation		
Number of Grt crystals investigated	1749	1256
Minimum Grt diameter (μm)	20	20
Maximum Grt diameter (μm)	255	250
Average Grt diameter (μm)	116	109
Number of Grt/mm^3	113	111
Grt (vol. %) calculated	12·9	11·2

30 μm (Tables 1–3). Both domains contain accessory apatite, rutile, ilmenite, zircon and allanite.

P-domain

The P-domain is dominated by plagioclase (c. 63 vol. %), which occurs together with quartz, garnet, biotite, and minor muscovite and chlorite (Table 1). Muscovite is either occluded by plagioclase or is intergrown with biotite, chlorite and euhedral garnet. The latter observation indicates that muscovite and chlorite are in equilibrium with plagioclase, biotite and garnet, and were not formed during retrogression. In most places, plagioclase forms an equigranular matrix of round to slightly elongated grains, which have a maximum size of c. 300 μm. In addition, sub- to anhedral plagioclase grains are irregularly intergrown with quartz, biotite, muscovite and chlorite (Fig. 3a and b). Garnet in the P-domain occurs along grain boundaries, often at plagioclase and plagioclase–quartz triple point junctions, except for a few grains that are completely overgrown by biotite.

B-domain

The B-domain has nearly the same assemblage as observed in the P-domain, but the biotite mode is much higher (c. 23 vol. %), and muscovite is very rare (<0·1 vol. %; Table 1). The quartz and plagioclase textures are similar to the P-domain with

Table 2: *Analyses of garnet from the P- and B-domains (in wt %)*

Sample:	P221 core-c	P221 core-r	P221 rim	B178 core-r	B178 rim	B125 core-c	B125 core-r	B125 rim	B339 core-c	B339 core-r	B339 rim	P388 core-c	P388 core-r	P388 rim	B42 core-c	B42 rim	B39 core-c	B39 core-r
Diameter:	255	255	255	126	126	81	81	81	207	207	207	137	137	137	160	160	112	112
SiO_2	35·65	35·73	36·47	35·94	36·80	35·74	35·92	36·71	35·81	36·15	36·79	35·66	36·05	36·66	35·97	36·40	36·07	36·28
TiO_2	0·16	0·19	<0·05	0·18	0·08	0·15	0·20	0·08	0·13	0·24	0·06	0·18	0·14	<0·05	0·15	0·22	0·13	<0·05
Al_2O_3	20·63	20·69	21·40	20·31	21·19	20·40	20·58	21·10	20·64	20·52	21·22	20·61	20·66	21·01	20·49	20·74	20·51	20·90
Fe_2O_3	0·96	2·02	1·49	1·99	0·87	0·77	2·22	1·69	1·34	1·56	0·50	1·48	2·13	1·59	0·76	0·77	0·64	1·95
Y_2O_3	0·92	<0·08	<0·08	<0·08	<0·08	0·85	<0·08	<0·08	1·10	<0·08	<0·08	1·13	<0·08	<0·08	0·82	0·12	0·91	<0·08
MgO	0·42	0·33	2·20	1·10	2·12	1·37	1·23	2·53	0·54	0·42	2·36	0·64	0·63	2·32	0·91	2·13	1·27	1·30
CaO	3·98	4·51	4·73	4·72	4·77	3·94	4·55	4·75	3·74	4·62	5·50	3·96	4·79	4·69	3·75	4·50	3·78	3·67
MnO	22·10	22·49	8·30	15·01	5·88	13·97	14·11	9·65	20·53	20·54	7·83	18·52	18·19	8·38	19·03	10·21	14·47	14·70
FeO	14·54	13·74	25·26	19·93	28·22	21·24	20·82	23·60	16·39	15·98	24·87	17·84	17·55	25·24	17·45	23·83	21·48	21·52
Sum	99·36	99·70	99·85	99·18	99·93	98·43	99·63	100·11	100·22	100·03	99·13	100·02	100·14	99·89	99·33	98·92	99·26	100·32
oxygens	24	24	24	24	24	24	24	24	24	24	24	24	24	24	24	24	24	24
Si	5·877	5·854	5·873	5·893	5·927	5·909	5·860	5·892	5·861	5·900	5·943	5·846	5·870	5·860	5·913	5·929	5·921	5·880
Ti	0·020	0·023	b.d.	0·023	0·010	0·018	0·025	0·010	0·016	0·030	0·007	0·022	0·017	b.d.	0·019	0·027	0·016	b.d.
Al	4·008	3·996	4·062	3·924	4·022	3·975	3·958	3·992	3·983	3·947	4·040	3·982	3·965	3·959	3·970	3·982	3·968	3·992
Fe^{3+}	0·119	0·250	0·181	0·245	0·106	0·096	0·273	0·204	0·166	0·192	0·061	0·182	0·261	0·192	0·094	0·095	0·079	0·238
Y	0·080	b.d.	b.d.	b.d.	b.d.	0·075	b.d.	b.d.	0·096	b.d.	b.d.	0·099	b.d.	b.d.	0·071	0·010	0·079	b.d.
Mg	0·103	0·081	0·529	0·268	0·510	0·338	0·299	0·606	0·132	0·101	0·568	0·157	0·152	0·553	0·224	0·517	0·310	0·313
Ca	0·702	0·792	0·817	0·830	0·824	0·698	0·796	0·817	0·655	0·809	0·951	0·695	0·836	0·803	0·660	0·785	0·665	0·638
Mn	3·085	3·121	1·132	2·085	0·802	1·956	1·950	1·311	2·847	2·840	1·071	2·571	2·510	1·135	2·649	1·409	2·012	2·018
Fe^{2+}	2·005	1·883	3·402	2·733	3·801	2·936	2·840	3·168	2·243	2·181	3·360	2·446	2·390	3·373	2·399	3·246	2·949	2·916
Sum	16·000	16·000	16·000	16·000	16·000	16·000	16·000	16·000	16·000	16·000	16·000	16·000	16·000	16·000	16·000	16·000	16·000	16·000
X_{alm}	0·336	0·320	0·579	0·462	0·640	0·489	0·483	0·537	0·376	0·368	0·565	0·410	0·406	0·575	0·400	0·544	0·490	0·496
X_{prp}	0·017	0·014	0·090	0·045	0·086	0·056	0·051	0·103	0·022	0·017	0·095	0·026	0·026	0·094	0·037	0·087	0·052	0·053
X_{sps}	0·516	0·531	0·193	0·352	0·135	0·326	0·331	0·222	0·477	0·479	0·180	0·431	0·426	0·194	0·441	0·236	0·334	0·343
X_{grs}	0·118	0·135	0·139	0·140	0·139	0·116	0·135	0·138	0·110	0·136	0·160	0·116	0·142	0·137	0·110	0·132	0·111	0·108
X-YAG	0·013					0·012			0·016			0·017			0·012	0·002	0·013	

X_{alm} = Fe^{2+}/FMCMnY; X_{prp} = Mg/FMCMnY; X_{sps} = Mn/FMCMnY; X_{grs} = Ca/FMCMnY; X-YAG = Y/FMCMnY; FMCMnY = Fe^{2+} + Mg + Ca + Mn + Y; core-c, Y_2O_3-rich centre of garnet cores; core-r, Y_2O_3-poor margins of garnet cores; rim, garnet rim. Fe_2O_3 contents were recalculated by charge balance. b.d., element below the detection limit, not used for mineral formula calculation.

respect to grain shapes and sizes (Fig. 3c and d), but there are more grain boundaries with biotite. The biotite flakes are much larger (up to 1 mm in length or width) than the quartz and plagioclase crystals (Fig. 3c and d).

Garnet textures

Garnet shape and spacing

Garnet grains in all domains are euhedral, with very few exceptions (≪ 1%), and show typical rhomb-dodecahedral {110} shapes. This is evident from thick-section observations as well as from a heavy mineral concentrate obtained from the gneiss sample. As a result of this geometry the garnet grains are considered as spheres in the following calculations. Most garnet grains form single, isolated crystals (*c*. 95% of the garnet population), which are separated from the next garnet grain by a space of about one garnet diameter or less (Fig. 3). The remaining 5% form clusters or aggregates of two or more garnet grains that either show point contacts or are closely intergrown. Intergrown garnet grains can have identical diameters but more commonly show different sizes.

Garnet mode and crystal size distribution

Garnet mode, absolute grain size, and CSDs were investigated in both domains, using the methods described in Appendix A. Crystal size analyses of garnet grains in the thick section (Appendix A) and point counting analyses of the final thin section yielded nearly identical garnet modes for the P- and B-domains (Table 1; 11–12 vol. %). This result is surprising if we consider that the local bulk-rock

Table 3: Mineral analyses of the P- and B-domains (in wt %)

Domain:	B	B	B	P	P	P	P	B	P	B	P
Mineral:	Pl	Pl	Pl	Pl	Pl	Pl	Bt	Bt	Chl	Chl	Ms
	av.	core	rim	av.	core	rim	av.	av.	av.	av.	av.
	$n = 92$			$n = 98$			$n = 18$	$n = 23$	$n = 7$	$n = 17$	$n = 8$
SiO_2	61·96	60·63	63·31	62·48	61·83	63·54	36·67	37·44	25·82	25·84	43·93
TiO_2	—	—	—	—	—	—	1·80	2·12	<0·06	<0·06	0·68
Al_2O_3	24·09	24·84	22·98	23·93	23·96	23·07	18·03	18·75	20·77	20·79	34·64
Cr_2O_3	—	—	—	—	—	—	<0·07	0·08	<0·07	<0·07	<0·07
Fe_2O_3	0·21	0·23	<0·10	0·26	0·10	<0·10	—	—	0·24*	0·00*	—
FeO	—	—	—	—	—	—	15·44	14·74	23·23	23·20	1·15
MgO	<0·09	<0·09	<0·09	<0·09	<0·09	<0·09	13·36	13·11	16·13	16·00	1·08
MnO	—	—	—	—	—	—	0·37	0·41	1·23	1·08	<0·08
CaO	5·30	6·20	4·03	4·77	5·29	4·04	<0·10	<0·10	<0·10	<0·10	<0·10
BaO	<0·08	<0·08	<0·08	<0·08	<0·08	<0·08	<0·08	<0·08	—	—	2·89
Na_2O	8·55	8·14	9·41	8·85	8·67	9·33	0·14	0·18	0·20	0·20	1·07
K_2O	0·08	0·07	<0·07	0·08	<0·07	0·07	8·48	8·54	<0·07	0·12	8·55
Sum	100·19	100·11	99·73	100·37	99·85	100·05	94·29	95·37	87·61	87·23	93·99
oxygens	8	8	8	8	8	8	22	22	†	†	22
Si	2·742	2·695	2·803	2·757	2·745	2·804	5·507	5·529	5·414	5·437	6·037
Ti	—	—	—	—	—	—	0·203	0·235	b.d.	b.d.	0·070
Al	1·257	1·301	1·199	1·245	1·254	1·200	3·191	3·263	5·133	5·156	5·610
Cr	—	—	—	—	—	—	b.d.	0·009	b.d.	b.d.	b.d.
Fe^{3+}	0·007	0·008	b.d.	0·009	0·003	b.d.	—	—	0·038	0·000	—
Fe^{2+}	—	—	—	—	—	—	1·939	1·820	4·073	4·083	0·132
Mg	b.d.	b.d.	b.d.	b.d.	b.d.	b.d.	2·991	2·886	5·042	5·018	0·221
Mn	—	—	—	—	—	—	0·047	0·051	0·218	0·192	b.d.
Ca	0·251	0·295	0·191	0·226	0·252	0·191	b.d.	b.d.	b.d.	b.d.	b.d.
Ba	b.d.	b.d.	b.d.	b.d.	b.d.	b.d.	b.d.	b.d.	—	—	0·156
Na	0·734	0·701	0·808	0·757	0·746	0·798	0·041	0·052	0·081	0·082	0·285
K	0·004	0·004	b.d.	0·004	b.d.	0·004	1·591	1·559	b.d.	0·032	1·438
Sum	4·995	5·004	5·001	5·001	5·000	4·997	15·510	15·405	20·000	20·000	13·949
F/FM	0·00	0·00	0·00	0·00	0·00	0·00	0·39	0·39	0·45	0·45	0·37
X_{ab}	0·74	0·70	0·81	0·77	0·75	0·80					
X_{an}	0·25	0·29	0·19	0·23	0·25	0·19					

$F/FM = Fe^{2+}/(Fe^{2+} + Mg)$; $X_{ab} = Na/(Na + Ca + K)$; $X_{an} = Ca/(Na + Ca + K)$; av., average of n analyses, Pl, plagioclase; Bt, biotite; Chl, chlorite; Ms, muscovite; —, element not analysed; b.d., element below the detection limit, not used for mineral formula calculation.
*Fe_2O_3 recalculation according to Zeh & Millar (2001).
†Normalized to 20 cations.

compositions, as reflected by modes and compositions of coexisting phases, are very different in the two domains (Table 1).

Garnet CSDs were obtained by measuring a total of 1749 grains in the P-domain and 1256 grains in the B-domain volume (Appendix A). The results indicate that garnet grains in both domains show nearly identical size spreads (20–255 μm) and average garnet abundances of 111–113 Grt/mm^3 (Table 1). A frequency vs diameter diagram (Fig. 4) shows that the grain number steadily increases from *c.* 250 μm to 110 μm, and then decreases towards smaller sizes until 20 μm. As 10 regular size classes were used to display the CSD in Fig. 4, the maximum (255 μm) and minimum (20 μm) sizes of individual garnet grains cannot be shown.

From the textural results it can be concluded that the nucleation density in the P- and B-domains was nearly identical, assuming that each existing garnet grain grew from a single nucleus. The CSD may suggest that the
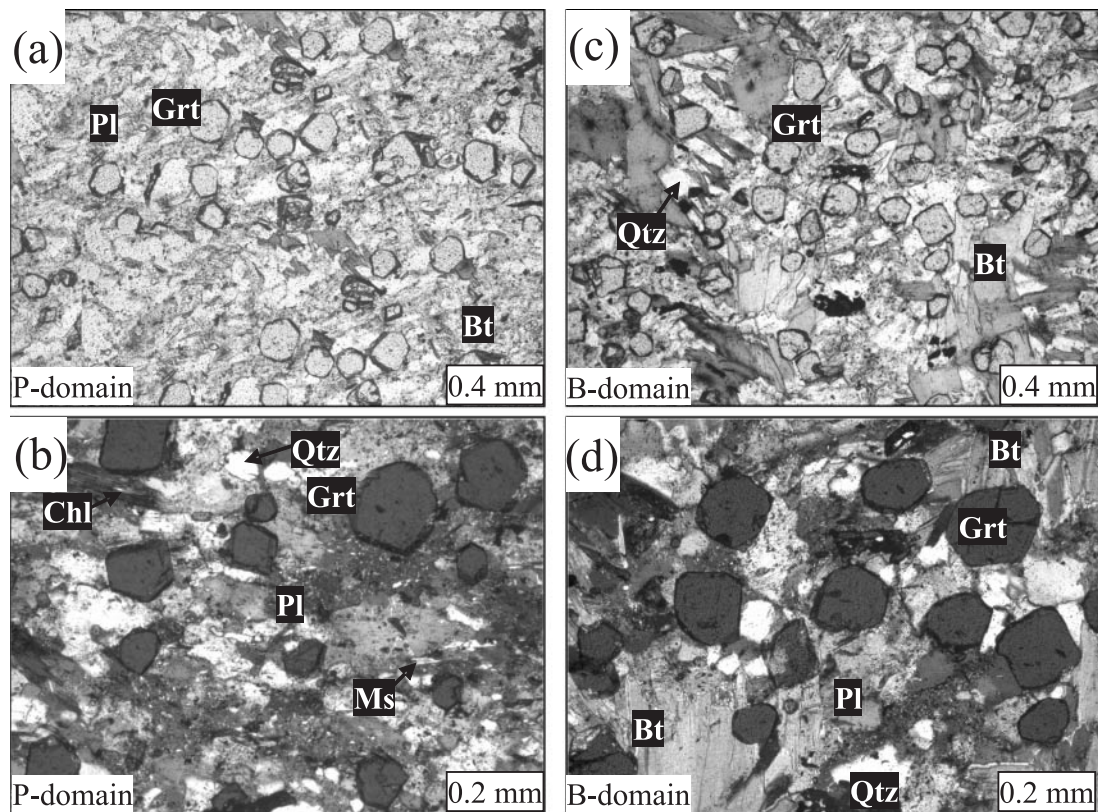
Fig. 3. Microphotographs showing garnet and associated matrix minerals in the P-domain (a, b) and in the B-domain (c, d). (a, c) photographed in transmitted light; (b, d) photographed with nearly crossed Nicols. Pl, plagioclase; Grt, garnet; Bt, biotite; Ms, muscovite; Chl, chlorite; Qtz, quartz.

garnet nucleation rate increased more or less continuously at the beginning of the garnet growth evolution and then decreased. However, this conclusion holds true only for the case that (1) larger garnet grains nucleated prior to smaller ones, and (2) garnet grains of different sizes in all domains grew with a similar radial growth rate at each step of the garnet growth history (Kretz, 1966; Carlson, 1989). In the next section it will be shown that both of the above requirements are fulfilled in the investigated domains, although there are some exceptions.

MINERAL CHEMISTRY
Matrix minerals

Point analyses and zonation profiles were measured with an electron microprobe (Appendix A) on all rock-forming minerals in both domains. Biotite grains in the P- and B-domains have identical average X_{Fe} [X_{Fe} = Fe/(Fe + Mg)] of 0·39. However, the biotite flakes of the P-domain have slighty lower Al^{tot}, Ti and Mn contents than those of the B-domain (Table 3). Chlorite in both domains shows similar average X_{Fe} (0·45), Al^{VI} (2·56–2·59 p.f.u.) and Mn^{VI} (0·19–0·22 p.f.u.) contents. Muscovite, observed only in the P-domain, has an

average silica content of Si = 6·02 p.f.u. and an average Na/(Na + K) value of 0·16. Plagioclase crystals in both domains are typically unzoned, although the total plagioclase population varies in composition between X_{an} = 0·19 and X_{an} = 0·29 [X_{an} = Ca/(Ca + Na)] in the B-domain and X_{an} = 0·19 and X_{an} = 0·25 in the P-domain. The few zoned plagioclase crystals show an increase in X_{an} from core to the rim from 0·25 to 0·29 in the B-domain, and from 0·19 to 0·20 in the P-domain. As plagioclase is the only Ca-bearing mineral beside euhedral garnet grains, it can be concluded that the anorthite content in plagioclase decreased during garnet growth. Average plagioclase compositions, as used for the calculations below, were obtained from about 100 regularly spaced (spacing *c.* 40 μm) point analyses measured in both domains (Table 3). The results indicate an average plagioclase composition of $An_{23}Ab_{77}$ for the P-domain and of $An_{25}Ab_{75}$ for the B-domain. Small ilmenite crystals occur only as inclusions in garnet of both domains, but never in the matrix. These ilmenite grains have high pyrophanite contents of 11–17 mol % and low haematite contents of <1 mol %. In contrast, almost stoichiometric rutile typically occurs near the rim of some garnet grains and abundantly in the matrix.
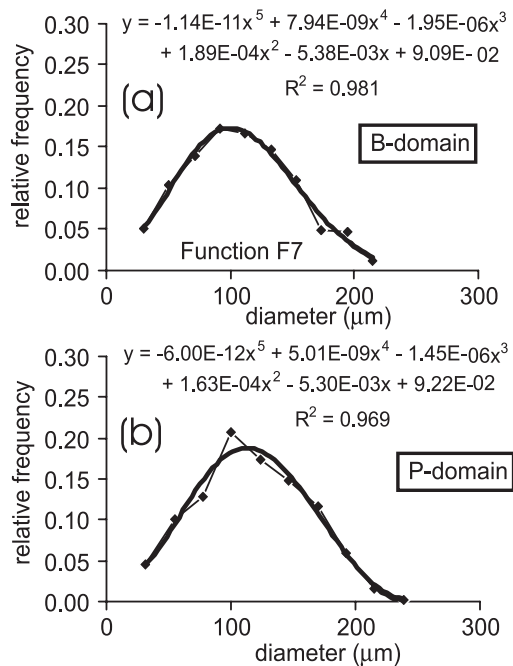
Fig. 4. Relative frequency vs garnet size diagram for garnet grains from the B-domain (a) and P-domain (b). The curves were fitted with EXCEL®. The corresponding power functions are shown.
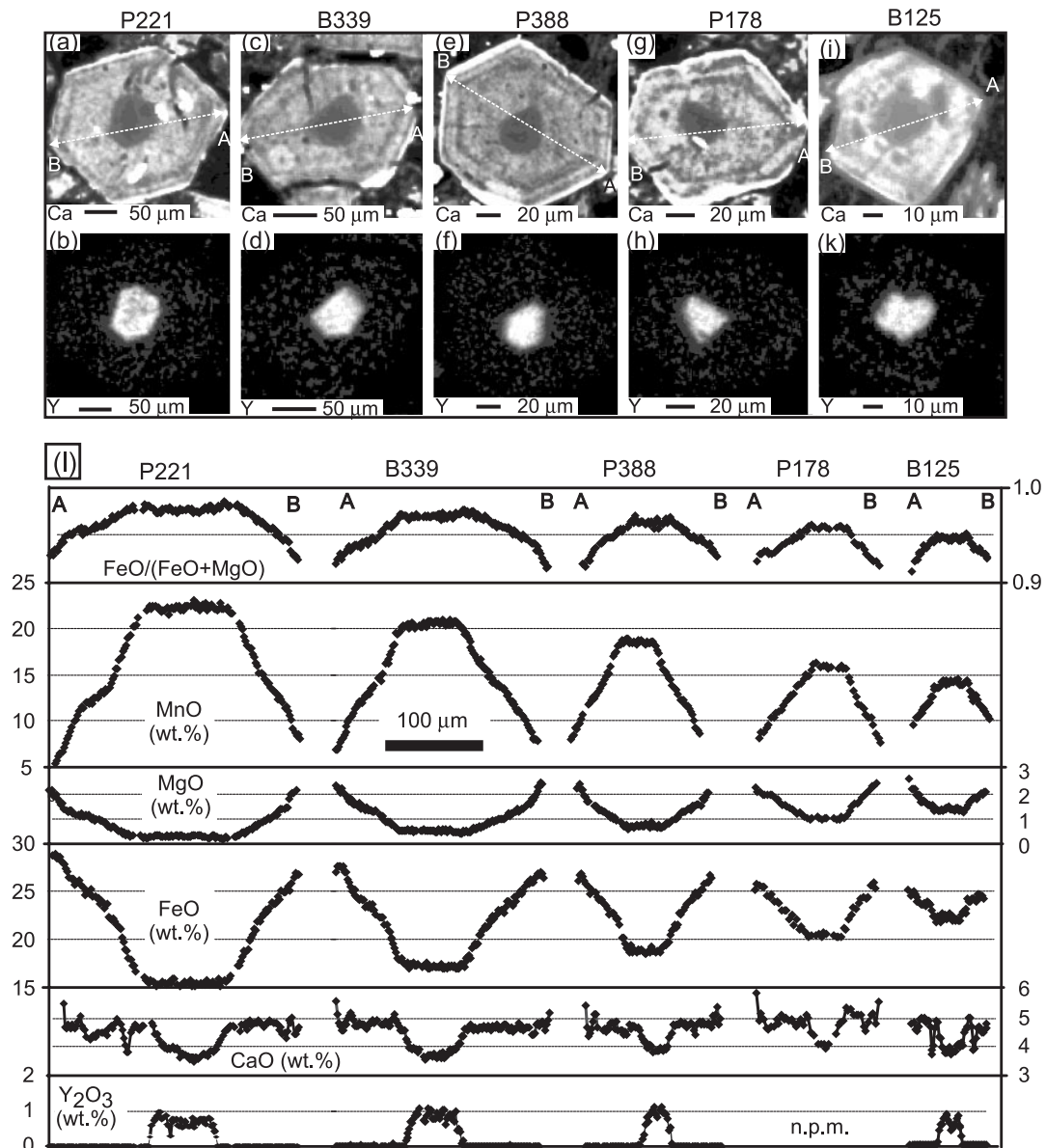
Garnet

Garnet zonation profiles were measured on centrally cut garnet grains that were carefully selected during thick-section preparation and investigation (Appendix A). To obtain information about the 2-dimensional element distribution, X-ray maps were also produced (Fig. 5a–k). The zonation patterns of the garnet porphyroblasts from the B- and P-domains, as revealed by these maps, show many similarities, indicating that the garnet growth evolution in both domains must have been nearly identical. The most pronounced feature is that all garnet grains are manganese-rich and unzoned with respect to MnO and FeO in their cores but are strongly zoned towards their rims (Fig. 5l). In fact, the MnO zonation of all garnet grains shows a typical flat-top geometry (referred to below as 'flat-top garnet'). In contrast to MnO and FeO, the MgO content decreases slightly toward the margin of the flat-top core, and then increases toward the garnet rim. Consequently, the FeO/(FeO + MgO) ratio first increases and then decreases (Fig. 5). Another important feature is that the cores of all flat-top garnet grains, regardless of their size, contain high Y_2O_3 contents between 0·82 and 1·1 wt % (Figs 5 and 6; Table 2), which drop below the detection limit of the electron microprobe (*c.* 0·1 wt %) near the transition from the flat-top garnet core to the zoned rim. Generally, the Y_2O_3 content drops below the detection limit before the MnO content starts to decline. Thus, the

flat-top core is divided into an Y_2O_3-rich inner domain and a thin Y_2O_3-free outer domain, which both have the same MnO contents. As shown in Fig. 5, the rapid decrease of Y_2O_3 is compensated by an increase of CaO. This indicates that Y in the garnet core is mainly substituted by Ca, perhaps by the coupled substitution $Ca^{2+[8]}Si^{4+[4]} \leftrightarrow Y^{3+[8]}Al^{3+[4]}$.

Laser ablation–inductively coupled plasma–mass spectrometry (LA–ICP–MS) measurements (Appendix A) indicate that the Y content of the zoned garnet overgrowths is on average 200 ppm. Backscattered electron (BSE) images and time-resolved LA–ICP–MS analyses additionally reveal that garnet grains with Y_2O_3-rich cores occur in close proximity to each other (Fig. 6a and b), and that most (if not all) garnet grains have Y_2O_3-rich cores (Figs 5 and 6). The latter is supported by time-resolved LA–ICP–MS analyses, which were carried out on 20 garnet grains from a very restricted rock volume (Fig. 6b). These porphyroblasts were 'drilled' with the laser for 90 s, while the evaporated material was time-resolved monitored for the two isotopes ^{55}Mn and ^{89}Y. This method allows discrimination between different garnet zones and the matrix (Fig. 6c). Y_2O_3-rich garnet cores always yield the highest ^{55}Mn signal, and show ^{89}Y counting rates of >0·4 × 10^4 counts/10 ms, even for the case that the Y_2O_3-rich garnet cores were not perfectly hit by the laser or were smaller than the laser spot diameter of *c.* 30 μm. In contrast, the ^{89}Y counting rate of Y_2O_3-poor overgrowths never exceeded 0·5 × 10^4 counts/10 ms (Fig. 6c); this counting rate was carefully tested on garnet grains that were characterized by microscopy and BSE images prior to their analysis; for example, grains 8, 11, 12, 13 in Fig. 6b.

Away from the flat-top cores, all garnet grains show a significant decrease of the MnO content toward the rim (Figs 5 and 7). However, the slope of the MnO zonation (ΔMnO/Δlength) is not steady, but shows two significant kinks in the range between 15 and 12 wt % (Figs 5 and 7), where the slope becomes more shallow (Fig. 7a). This change in slope can be observed in nearly all garnet grains that have MnO contents >12 wt % (Fig. 5), and is reflected in the MnO slope vs MnO content diagram in Fig. 7b. It should be noted that the observed change in slope, in conjunction with the observed flat-top geometry, cannot be explained by a Rayleigh fractionation model. Figure 7b also shows that garnet grains with different sizes have, away from their flat-top cores, nearly identical MnO slopes throughout the garnet growth history. This indicates that all garnet grains, after formation of their individual flat-top cores, underwent nearly the same radial growth at each time during the formation of their zoned overgrowths. Nevertheless, there are small deviations from this general trend. These are reflected by small differences in the MnO slopes

Fig. 5. X-ray maps (a–k) and zonation profiles (l) of garnet grains from the P- and B-domains. The profiles A–B in the X-ray maps correspond to the profiles shown below. (a, c, e, g, i) Ca-maps; (b, d, f, h, k) Y-maps; n.p.m., no quantitative profile measured.

between garnet grains (Fig. 7a and b). Moreover, such deviations can also be observed on single garnet grains. For example, the MnO slopes between the right and left flanks of the garnet grain P221 (Fig. 5) are not mirror images of each other. This particular grain shows significant deviations in the MnO slope in the range below 15 wt % MnO (Figs 5 and 8g). In contrast to MnO, FeO and MgO, the CaO content remains nearly constant (*c.* 4·5–5·0 wt %) away from the flat-top cores, except a few rims with CaO contents up to 6·0 wt %. However, in some grains, asymmetric depletions in CaO are noted on opposing sides of any given grain, as shown

by the zonation profiles and X-ray maps in Fig. 5 (e.g. garnet P221). These spatially uncorrelated depletions in CaO may result from kinetic effects (see Chernoff & Carlson, 1997).

Figures 5 and 7 also show that the rim composition of the investigated garnet grains is not identical but scatters with MnO concentrations between 5·5 and 10 wt %. Such variations occur between garnet grains, but also at different edges of single, euhedral garnet porphyroblasts (e.g. grain P221; Fig. 5). This indicates that the growth of garnet porphyroblasts and/or of different garnet edges either stopped at different times and/or that chemical
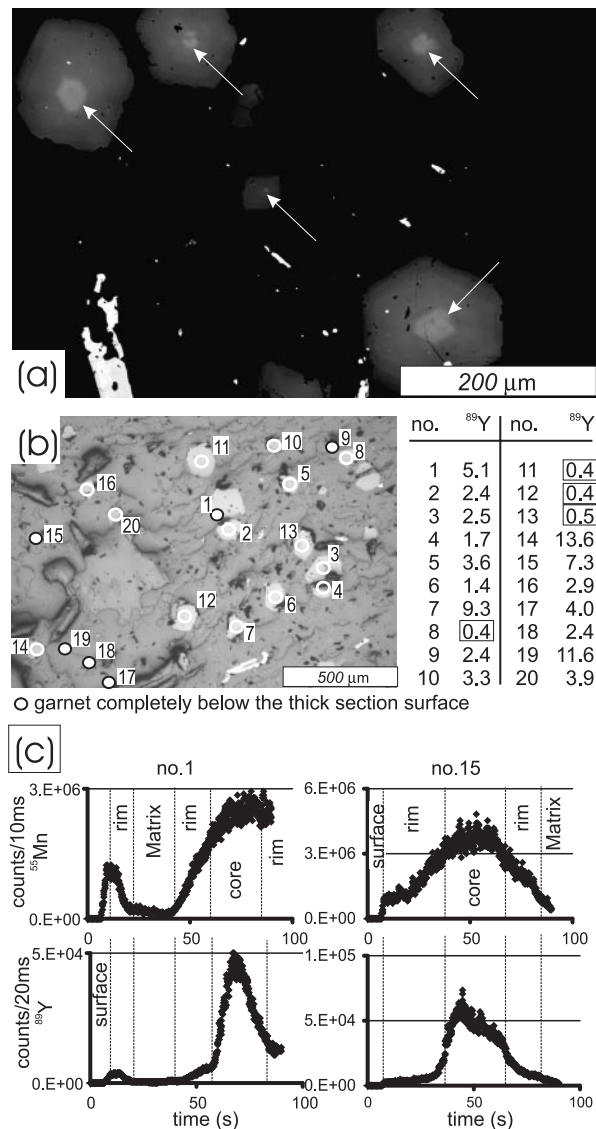
Fig. 6. (a) BSE image of a thick-section surface showing garnet porphyroblasts with Y_2O_3-rich cores (white arrows), which occur in close proximity to each other. (b) Reflected light microphotograph of a thick section showing the distribution of garnet grains, which were analysed by time-resolved LA–ICP–MS analysis. To the right the maximum ^{89}Y signals (in counts/10 ms × 10^5) obtained for the respective laser spots are shown. The boxes mark spots where no Y_2O_3-rich garnet core was detected. In these spots the laser penetrated garnet relics whose cores had been ground away, as supported by BSE images and microscopy. (c) Counts vs time diagrams showing the time-resolved, uncorrected signals of the isotopes ^{55}Mn and ^{89}Y, which were monitored during a 90 s time interval while the laser was drilling into the thick section. The signal evolution in diagram 1 shows that the laser first penetrated the rim of a garnet grain exposed at the thick-section surface (low ^{89}Y signal), then a matrix mineral (low ^{89}Y signal), then the rim of a second garnet grain below the thick-section surface (low ^{89}Y signal), and finally the core of this second garnet grain (high ^{89}Y signal, highest ^{55}Mn signal). Profile 15 shows the ^{89}Y and ^{55}Mn signals monitored while the laser was 'drilling' through a single garnet grain, which occurs directly below the thick-section surface. The garnet core is well characterized by the sharp increase and decrease of the ^{89}Y signal, and the highest ^{55}Mn signal.
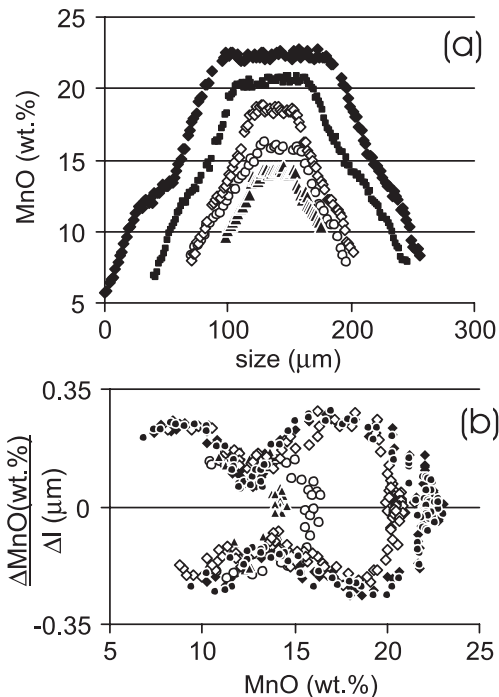

Fig. 7. (a) Synopsis of MnO zonation profiles measured on centrally cut garnet grains of different size. These profiles correspond to Fig. 5. (b) MnO zonation slope (= $\Delta MnO/\Delta l$) vs MnO content diagram. The symbols in (b) correspond to those in (a). (For further explanation see text.)

equilibrium was not maintained on millimetre scale throughout the garnet growth history.

GARNET SIZE–COMPOSITION RELATIONSHIPS

Careful investigations of 17 centrally cut garnet grains (Appendix A) indicate that the MnO content of the flat-top garnet cores decreases systematically with the garnet size (Fig. 8e), i.e. larger garnet grains have higher MnO contents in their cores than smaller ones. This correlation [function (F5) in Fig. 8e], and the fact that the zoned overgrowths of garnet grains of different sizes formed with similar radial growth rates at each time (see above), provide unambiguous evidence that the MnO content can be used as a time line (see Daniel & Spear, 1999). This means that garnet grains with higher MnO contents in their flat-top cores formed earlier than garnet grains with lower MnO contents. The textural investigations also show a positive correlation between the garnet size and the size of the flat-top garnet cores [function (F6) in Fig. 8f], i.e. smaller garnet grains have smaller flat-top cores than larger grains. By combination of the functions (F5) and (F6) the MnO content can be related to the garnet core size.
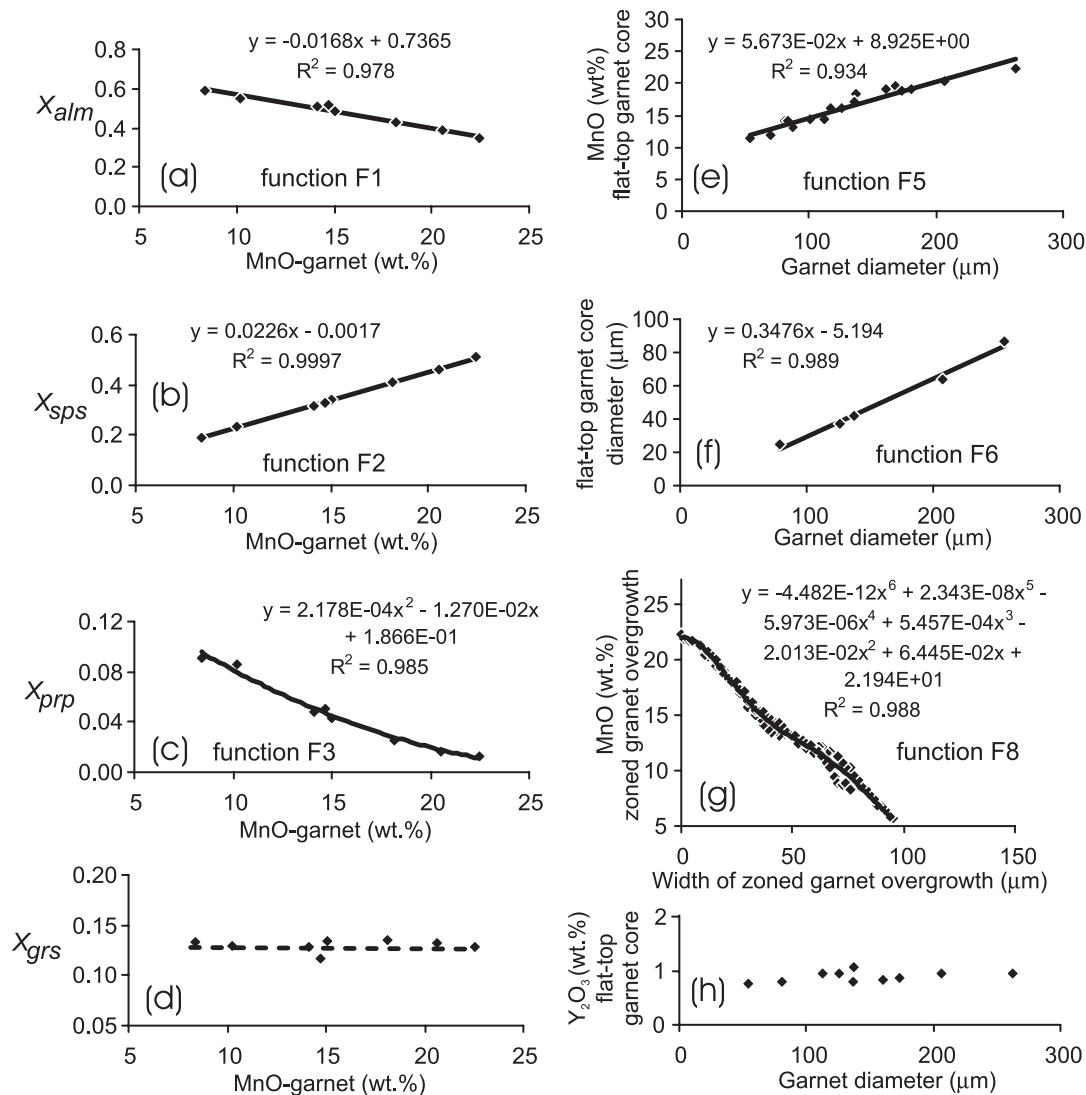
Fig. 8. Functions fitted from textural and compositional parameters inferred from the investigated rock domains. The fits and the related power functions are obtained with the software EXCEL®. (a) Function (F1): X_{alm} vs MnO content; (b) function (F2): X_{sps} vs MnO content; (c) function (F3): X_{prp} vs MnO content; (d) X_{grs} vs MnO content; (e) function (F5): MnO content of flat-top garnet cores vs garnet diameters; (f) function (F6): diameter of flat-top garnet cores vs garnet diameter; (g) function (F8): MnO content of garnet vs the width of zoned garnet overgrowth; (h) Y_2O_3 content of flat-top garnet cores vs garnet diameter (obtained on centrally cut garnet grains). The compositional relationships in (a–d) were derived using the core compositions of seven centrally cut garnet grains at their Y_2O_3-poor margins (Table 2). For the point with the lowest MnO content a garnet rim composition was used. The relationships in (f) were derived from five centrally cut garnet grains, which showed euhedral Y_2O_3-rich garnet cores in BSE images. The relationship in (g) was estimated by fitting the MnO zonation profiles of the left and right flank of the largest garnet grain (P221, Fig. 5). (For further explanation see text.)

The garnet composition data show that for a certain MnO content the composition of a flat-top garnet core (at its Y_2O_3 free margin) is nearly identical to the rim composition of a zoned garnet overgrowth, which is formed around an earlier nucleated garnet grain. This implies that the flat-top cores of smaller garnet grains, in particular their Y_2O_3-free margins, simultaneously formed in the same chemical environment as the overgrowths of larger garnet grains. Thus the MnO content can be used to correlate the composition during the formation of the flat-top garnet cores with the composition of the overgrowths around earlier formed garnet grains.

The radius gain during formation of the zoned garnet overgrowth can be calculated by means of function (F8), which correlates the garnet overgrowth width with the MnO content of the largest garnet grain (Fig. 8g). It should be noted that function (F8) reflects an average garnet overgrowth zonation profile, which results from the fact that the garnet growth zonation around single

garnet grains is not perfectly radially symmetrical, as mentioned above. Because the zoned overgrowth around garnet grains of different sizes formed at nearly the same radial growth rate (see above), function (F8) is sufficient to calculate the radial gain around all garnet grains.

INTERPRETATION OF THE FLAT-TOP GARNET ZONATION PATTERNS

The positive correlation between the MnO content of garnet cores and the garnet diameter (Fig. 8e), together with the similar garnet overgrowth zonation patterns (Fig. 7), hints that the garnet population in the investigated rock sample formed during a single metamorphic process, driven by at least one multivariant mineral reaction. In this context the observed flat-top garnet geometry needs some explanation. In general, it could result from several processes, e.g. from a kinetically controlled initial garnet growth after a significant amount of reaction overstep (unzoned core: Zeh & Holness, 2003) followed by equilibrium garnet growth (zoned overgrowth), by an abrupt increase of the garnet nucleation density during equilibrium garnet growth (Zeh & Millar, 2001), and/or by kinetic effects, which were triggered by trace element incorporation into garnet. The observation that all flat-top garnet cores contain high Y_2O_3 contents (up to 1·0 wt %; Figs 5 and 8h) may indicate that nucleation and initial garnet growth was triggered by Y_2O_3. Furthermore, the abrupt decrease of the Y_2O_3 content below the detection limit at the flat-top garnet core–zoned garnet overgrowth transition (Fig. 5) may indicate that the incorporation of Y into garnet was controlled by kinetic factors such as transport and/or surface kinetics (e.g. Hickmock & Shimizu, 1990; Watson, 1996; Lanzirotti, 1995), which were relatively unimportant for the incorporation of the major elements MnO, FeO, MgO, CaO, Al_2O_3 and SiO_2.

A kinetically controlled, asynchronous, incorporation of Y_2O_3 into garnet is supported by the observation that garnet grains of different sizes and, thus, with different MnO core contents (Fig. 8e) occur in close proximity to each other (Figs 2, and 6a and b). In fact, the textural and compositional data require that Y_2O_3-rich flat-top cores of smaller garnet grains nucleated later than those of larger garnet grains, i.e. Y_2O_3-rich cores formed synchronously with Y_2O_3-poor overgrowths of larger grains. This observation requires that Y_2O_3 was either less effectively transported between adjacent garnet grains than the major elements or that surface processes caused a differential Y_2O_3 incorporation into adjacent garnet grains at the same time.

In this context it is interesting to note that similar features were observed in garnet growth experiments by Milke & Metz (2002), who investigated the reaction wollastonite + calcite + anorthite = grossular + CO_2. Because of the use of natural minerals the starting material in the experiments of Milke & Metz (2002) contained impurities of Fe_2O_3 (<0·5 wt %). These impurities meant that nearly all synthesized grossular crystals formed andradite-rich cores (up to 6·74 wt % Fe_2O_3), and andradite-poor overgrowth (maximum 0·77 wt % Fe_2O_3). These Fe_2O_3-rich cores were found in garnet grains of different sizes (2–36 μm; Milke & Metz, 2002). In further analogy to the study presented here, Milke & Metz (2002) showed that the andradite-rich cores formed asynchronously and in close proximity, i.e. the youngest Fe_2O_3-rich garnet cores nucleated and grew at the same time as the overgrowth of earlier, larger garnet grains by Fe_2O_3-poor rims. By comparison with these experiments I conclude that the formation of the Y_2O_3-rich flat-top garnet cores was kinetically controlled.

It is likely that the FeO/(FeO + MgO) increase toward the margins of the flat-top garnet cores also results from kinetic effects. In general, such an increase is interpreted to result from diffusive garnet alteration, caused by Fe–Mg exchange between garnet and surrounding minerals such as biotite (e.g. Florence & Spear, 1991; Hauzenberger et al., 2005). However, the garnet cores were successively formed and, as shown below, at relatively low temperatures (c. 470–550°C), which exclude such an interpretation. In fact, it is more likely that the individual cores were rapidly formed at constant P–T conditions. This is supported by the fact that the MnO and FeO contents in the flat-top garnet cores are nearly constant.

Identical slopes of the garnet MnO overgrowth zonation (Fig. 7) indicate that once an Y_2O_3-rich flat-top garnet core was formed, its further growth occurred with nearly the same radial growth rate as that of previously nucleated garnet grains. In fact, the identical garnet MnO slopes could be explained by a surface-controlled garnet growth mechanism, as suggested by Kretz (1974), Carlson (1989), and Daniel & Spear (1999). However, as shown by the data presented here, this garnet growth mechanism did not operate alone, but was accompanied by a second, perhaps trace element-controlled growth mechanism, responsible for the contemporaneous nucleation and fast growth of the flat-top garnet cores. In fact, these differences require that garnet cores and overgrowths are treated separately in the calculations carried out below.

In summary, the different lines of evidences point to the observed flat-top garnet cores having resulted from a fast, kinetically controlled garnet growth, perhaps initiated and triggered by the incorporation of Y_2O_3. In contrast, the contemporaneous formation of zoned garnet overgrowths was slower, pointing to a surface-controlled growth mechanism.

GARNET FRACTIONATION CALCULATION

Method

Element fractionation caused by garnet growth implies that a certain number of moles originally contained in the bulk rock is incorporated in the core of growing garnet grains and thus removed from the system. A general formulation, which allows the calculation of the number of moles of a system component i in a rock is (e.g. Spear, 1993)

$$m_i = \sum_{k=1}^{nph} M^k \sum_{j=1}^{npc^k} n_{i,j}^k X_j^k \qquad (1)$$

where m_i is the number of moles of each system component i in the rock ($i =$ MnO, MgO, etc.), M^k is the number of moles of phase k in the rock ($k =$ Pl, Bt, etc.), $n_{i,j}^k$ is the number of moles of system component i in one mole of each phase component j, X_j^k is the mole fraction of phase component j in the phase k($j = X_{an}^{Pl}, X_{ab}^{Pl}, X_{ann}^{Bt}$, etc.), nph is the number of phases, and npc^k is the number of phase components in phase k.

However, equation (1) can only be used if all phases in the considered rock are unzoned. If at least one phase is zoned, e.g. garnet, equation (1) must be modified as follows:

$$m_i = m_i^{ku} + m_i^{kz1} + \ldots + m_i^{kzn} \qquad (2)$$

where m_i^{ku} is the number of moles of each system component i of all unzoned phases ku in the rock. It can be calculated using equation (1), and for our specific problem by means of the parameters as explained in Appendix B. The terms $m_i^{kz1} \ldots m_i^{kzn}$ can be used to calculate the number of moles of each system component i in a number n of zoned phases kz. For each zoned phase

kz, m_i^{kz} can be calculated as follows:

$$m_i^{kz} = \sum_{s=1}^{n} M_s^{kz} \sum_{j=1}^{npc^{kz}} n_{i,j}^{kz} X_{j,s}^{kz} \qquad (3)$$

where M_s^{kz} is the number of moles in a zone (volume) of phase kz formed at a certain stage s, $n_{i,j}^{kz}$ is the number of moles of system component i in one mole of each phase component j of phase kz, and $X_{j,s}^{kz}$ is the mole fraction of phase component j in phase kz at a certain stage s.

Using equation (3) it is also possible to calculate the number of moles fractionated by a zoned mineral kz at a certain stage s, e.g. the moles of CaO, MgO, MnO, FeO, SiO$_2$, Al$_2$O$_3$ and Y$_2$O$_3$ during garnet growth. The number of moles of each system component i fractionated in the zoned phase kz at a certain stage s ($m_{i,s}^{kz}$) can be obtained as follows:

$$m_{i,s}^{kz} = m_i - \sum_{s=1}^{n} M_s^{kz} \sum_{j=1}^{npc^{kz}} n_{i,j}^{kz} X_{j,s}^{kz}. \qquad (4)$$

In this study garnet is considered to be the only zoned mineral. Additional zoning as, for example, observed in a few plagioclase crystals is not considered. Instead, an average plagioclase composition is used (see above). Thus there are only two terms on the right-hand side of equation (2). The second term is expressed by equation (3), which also forms the second term on the right-hand side of equation (4). Equation (4) can be solved when the terms for M_s^{Grt} and $X_{j,s}^{Grt}$ are known at each stage s of the garnet growth history. The term $n_{i,j}^{Grt}$ is defined by the fixed compositions of the garnet end-members almandine, spessartine, grossular, pyrope and YAG $=$ Y$_3$Al$_2$Al$_3$O$_{12}$ (e.g. 1 mole pyrope contains 3 moles MgO, 1 mole Al$_2$O$_3$ and 3 moles SiO$_2$). The evolution of a certain garnet population can easily be calculated using a t–s component matrix, as follows:

MnO (wt %)	$s = 1$ 22·5	2 21·2	3 19·8	4 18·5	5 17·2	6 15·9	7 14·6	8 13·3	9 12·0	10 10·7	11 9·4	12 8·1	Average diameter (µm)
$t = 1$	$s = t$	1,2	1,3	.	.	.	.	.	.	.	.	1,12	238·5
2		$s = t$	2,3	.	.	.	.	.	.	.	.	2,12	215·5
3			$s = t$	.	.	.	.	.	.	.	.	.	192·5
4				$s = t$	.	.	.	.	.	.	.	.	169·5
5					$s = t$	.	.	.	.	.	.	.	146·5
6						$s = t$	.	.	.	.	.	.	123·5
7							$s = t$	.	.	.	.	.	100·5
8								$s = t$	.	.	.	.	77·5
9									$s = t$	.	.	.	54·5
10										$s = t$	.	10,12	31·5

In this matrix t describes all garnet grains that belong to a certain size class, and each s describes a certain stage during the garnet growth evolution. The formation of the observed garnet population (Figs 4 and 5) was calculated using 12 discrete stages s ($s = 1–12$), which are defined by certain MnO contents (wt %) in garnet ($\text{MnO}_s^{\text{Grt}}$), e.g. $\text{MnO}_{s=1}^{\text{Grt}} = 22{\cdot}5$, $\text{MnO}_{s=2}^{\text{Grt}} = 21{\cdot}2$, $\ldots \text{MnO}_{s=12}^{\text{Grt}} = 8{\cdot}1$. Because the MnO content of the garnet cores increases linearly with the garnet size (Fig. 8e) the difference in MnO content between such steps was taken to be regular. In agreement with the petrographic observations, it is assumed that the formation (nucleation) of new garnet grains, belonging to a certain size class t, takes place during only the first 10 stages, until $\text{MnO}_{s=10}^{\text{Grt}} = 10{\cdot}7$. Afterwards garnet growth occurs without nucleation of any new garnet grains. In the calculations it is considered that all newly formed (nucleated) garnet grains at the stage $s = t$ are unzoned (flat-top), in agreement with the petrographic observations. Finally, it is assumed that at a stage s a garnet overgrowth (with $t < s$) has the same composition as the core of a newly formed garnet grain of size class t. This is in agreement with the compositional data obtained from the investigated garnet grains. Taking all this into account, the number of garnet moles formed at each stage s (M_s^{kz}) can be obtained as follows:

$$M_s^{\text{Grt}} = \frac{V_s^{\text{Grt}}}{v_s^{\text{Grt}}} \qquad (5)$$

where v_s^{Grt} is the volume of one mole garnet formed at stage s (cm³/mol) and V_s^{Grt} is the garnet volume formed at stage s (cm³).

It should be noted that the sum of all volumes V_s^{Grt} is equal to the garnet volume obtained by point counting (see Table 1). If we neglect excess volumes, v_s^{Grt} can be calculated according to

$$v_s^{\text{Grt}} = \sum_{j=1}^{nphc} X_{j,s}^{\text{Grt}} * v_j \qquad (6)$$

where $X_{j,s}^{\text{Grt}}$ is the mole fraction of phase component j ($X_{\text{alm}}, X_{\text{prp}}, X_{\text{sps}}, X_{\text{grs}}, X_{\text{YAG}}$) in garnet at stage s, and v_j is the molar volume of the phase component j.

The molar volumes of almandine, spessartine, grossular and pyrope are obtained from the thermodynamic dataset of Holland & Powell (1998) at standard conditions. The molar volume of YAG is assumed to be identical to that of grossular.

$X_{j,s}^{\text{Grt}}$ can be calculated using the functions (F1), (F2) and (F3), as shown in Fig. 8a–c, and the constraint $\sum X_{j,s}^{\text{Grt}} = 1$ (F4). The functions (F1)–(F3) relate the MnO content of garnet at each stage s ($\text{MnO}_s^{\text{Grt}}$) with the mole fractions of the phase

components j:

$$X_{\text{alm},s}^{\text{Grt}} = f(\text{MnO}_s^{\text{Grt}})_{\text{alm}} \qquad (\text{F1})$$

$$X_{\text{sps},s}^{\text{Grt}} = f(\text{MnO}_s^{\text{Grt}})_{\text{sps}} \qquad (\text{F2})$$

$$X_{\text{prp},s}^{\text{Grt}} = f(\text{MnO}_s^{\text{Grt}})_{\text{prp}} \qquad (\text{F3})$$

$$X_{\text{grs},s}^{\text{Grt}} = 1 - X_{\text{alm},s}^{\text{Grt}} - X_{\text{sps},s}^{\text{Grt}} - X_{\text{prp},s}^{\text{Grt}}. \qquad (\text{F4})$$

For the calculation of the garnet core composition the YAG component was considered as well. In agreement with the compositional data (Table 2) a fixed amount of $X_{\text{YAG}} = 0{\cdot}013$ was used, which substitutes for X_{grs}. Thus, for the garnet core calculation at each stage $s = t$ the function (F4) becomes

$$X_{\text{grs},s}^{\text{Grt}} = 1 - X_{\text{alm},s}^{\text{Grt}} - X_{\text{sps},s}^{\text{Grt}} - X_{\text{prp},s}^{\text{Grt}} - 0{\cdot}013. \quad (\text{F4a})$$

LA–ICP–MS analyses indicate that the YAG component of the garnet rims is, on average, c. 30 times smaller than that of the cores. Thus, for the calculation of the garnet rims, a fixed amount of $X_{\text{YAG}} = 0{\cdot}00043$ was used, and for the calculation of $X_{\text{grs},s}^{\text{Grt}}$ the function

$$X_{\text{grs},s}^{\text{Grt}} = 1 - X_{\text{alm},s}^{\text{Grt}} - X_{\text{sps},s}^{\text{Grt}} - X_{\text{prp},s}^{\text{Grt}} - 0{\cdot}00043. \quad (\text{F4b})$$

The garnet volume V_s^{Grt} formed at each stage s [used in equation (5)] can be calculated as follows:

$$V_s^{\text{Grt}} = V_{c,t=s}^{\text{Grt}} \times \mathcal{N}_t^{\text{Grt}} + \sum_{t=1}^{n=(t<s)} V_{o;t,s}^{\text{Grt}} \times \mathcal{N}_t^{\text{Grt}} \qquad (7)$$

where $V_{c,t=s}^{\text{Grt}}$ is the volume of the flat-top core of one garnet grain of size class t at stage $s = t$, $\mathcal{N}_t^{\text{Grt}}$ is the number of garnet grains of size class t, and $V_{o;t,s}^{\text{Grt}}$ is the volume of zoned overgrowth formed around one existing garnet of size class t at stage s.

The first product at the right-hand side of equation (7) gives the volume of all unzoned garnet cores formed at a certain stage $s = t$, and the second term gives the overgrowth volume formed around all garnet grains of all size classes t that nucleated prior to stage s.

The volume of the core of one garnet grain of size class t at stage s can be calculated as follows:

$$V_{c,t=s}^{\text{Grt}} = \frac{1}{6} \times \pi \times d_{c;t=s}^3 \qquad (8)$$

where $d_{c;t=s}$ is the diameter of the core of a garnet grain of size class t formed at stage s. This core diameter ($d_{c;t=s}$) can be calculated using the two functions (F5) and (F6), which are shown in Fig. 8e and f, as follows:

$$d_{c;t=s} = f(d_{t=s}^{\max}) \qquad (\text{F5})$$

$$\text{MnO}_s^{\text{Grt}} = f(d_{t=s}^{\max}). \qquad (\text{F6})$$

In these two functions $d_{t=s}^{\max}$ is the maximum diameter of a garnet grain of size class t, which started its growth

at stage $s = t$. The number of garnet grains of size class t (N_t^{Grt}) can be obtained from the function (F7), as shown in Fig. 4:

$$N_t^{\mathrm{Grt}} = f(d_t^{\max}). \qquad (F7)$$

The volume of overgrowth around one garnet t at a certain stage s ($V_{o;t,s}^{\mathrm{Grt}}$) can be calculated as follows:

$$V_{o;t,s}^{\mathrm{Grt}} = \frac{1}{6}\pi\left(d_{c;t=s} + \sum_{s>t}^{n} d_{o,s}\right)^3 \\ - \frac{1}{6}\pi\left(d_{c;t=s} + \sum_{s>t}^{n-1} d_{o,s}\right)^3 \qquad (9)$$

where $d_{o,s}$ is the diameter gain caused by new zoned garnet overgrowth between the stages s and $s - 1$. It can be calculated by

$$d_{o,s} = 2r_{o,s} - 2r_{o,(s-1)} \qquad (10)$$

where $r_{o,s}$ is the radius of the zoned garnet overgrowth at stage s, and $r_{o(s_{-1})}$, is the zoned garnet overgrowth radius at the previous stage $(s - 1)$. The two radii can be obtained by iteration of the function (F8) as shown in Fig. 8g:

$$\mathrm{MnO}_s^{\mathrm{Grt}} = f(r_{o,s}). \qquad (F8)$$

It is assumed that all garnet grains of size class t underwent the same radial growth at each stage s, except garnet cores formed at the stage $s = t$. Thus, the diameter gain (d_o,s) of all garnet grains at a certain stage s is identical. If this were not the case, the diameter gain (d_o,s) could be obtained by fitting functions for garnet grains of each size class t. Alternatively, if the radius–rate relationships follow special growth laws as described by Kretz (1974) or Carlson (1989), the diameter gain for garnet grains of different size classes t at each stage s should be obtained from these functions. Figure 9 shows the calculated MnO zonation profiles for garnet grains of all size classes t. These profiles are quite similar to the measured profiles as shown in Fig. 7a.

Finally it should be noted that the calculation procedure described above can only be used when the following prerequisites are fulfilled. First, the approach works only if all observed features (sizes, compositions, zonations) can be related to a time line, e.g. to the MnO content. If such a time line is not given, as shown by Hirsch et al. (2003) or Meth & Carlson (2005), the procedure cannot be used.

Second, the approach requires knowledge of how all crystal radii vary with time. Clearly, in most metamorphic rocks the radial variation of all garnet grains in a certain population may be difficult to access,
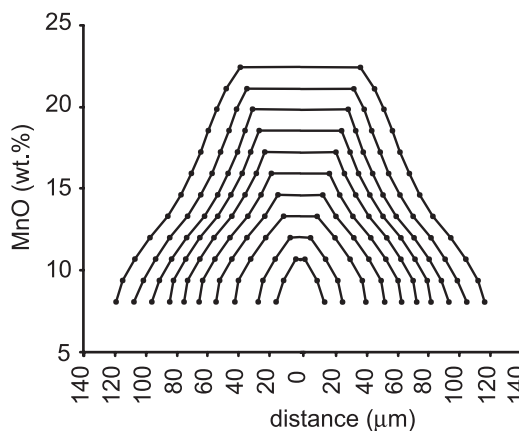

Fig. 9. Synthetic MnO zonation profile of garnet grains of different diameters, calculated with the parameters explained in the text.

in particular if the growth rate is not constant for all garnet grains at a certain time and if there is no simple relationship between garnet size and growth rate (see Carlson, 1989; Meth & Carlson, 2005). In the case studied, the reasonable approximation was made that the zoned overgrowths of all garnet grains grew with the same growth rate, and that the garnet core size decreased linearly with the garnet diameter [functions (F6) and (F7)].

Third, the method is most simple if, at any chosen point of time, all crystal are accreting identical compositions of material at their surface. Nevertheless, the method also allows the calculation for different rim compositions, i.e. the simultaneous formation of Y_2O_3-rich cores and Y_2O_3-poor overgrowths, as demonstrated above.

Results of garnet fractionation calculations

The bulk compositions prior to garnet growth and the extent of fractionation caused by garnet formation are calculated for the B- and P-domains (Tables 4 and 5). The unfractionated bulk compositions were calculated using the modes and compositions of all unzoned phases in the respective domains (Tables 1–3), and the CSDs, modes and zonation patterns of garnet, as described above (Figs 4 and 8; Table 2). For comparison, Table 4 also shows the bulk composition analysed by X-ray fluorescence (XRF; Appendix A) on two blocks of 20 mm × 30 mm × 5 mm size, taken in proximity to the thick section investigated. The results in Table 4 indicate some variation in the calculated and measured bulk compositions. These differences can be explained if the investigated rock consists of three general domains (P-, B- and quartz-rich domains), which are mixed to variable extent. In general, the B-domains contain more FeO, MgO and K_2O (required to form biotite) and

Table 4: Calculated and measured bulk composition

	B-domain (wt %)*	P-domain (wt %)*	XRF1 (wt %)†	XRF2 (wt %)†
SiO_2	63·82	60·33	62·49	61·08
TiO_2	0·72	1·45	0·95	0·88
Al_2O_3	13·85	18·96	16·96	16·05
FeO^{tot}	8·46	5·95	6·63	9·18
MgO	3·48	1·46	2·53	2·99
MnO	1·93	2·03	1·86	2·95
CaO	2·16	3·58	2·76	2·6
Na_2O	2·33	5·18	3·54	2·52
K_2O	2·26	0·67	2·04	1·92
H_2O	0·99	0·39	0·71‡	0·53‡
Sum	100·00	100·00	100·47	100·70
Y(ppm)	67	78	42	59

*Bulk composition reconstituted from mineral modes and compositions (see text).
†Bulk composition estimated by XRF on sample blocks of 30 mm × 20 mm × 5 mm size (see text).
‡Estimated by loss on ignition.

lower CaO, Na_2O and Al_2O_3 (required to form plagioclase) than the P-domains. Thus the compositional variations are in agreement with the thin-section observations. As shown in Table 4, the calculated Y content is slightly higher than the measured one. This can be explained by the fact that simplified garnet geometries and fixed Y values were used to calculate the composition of the garnet cores and rims.

Garnet fractionation in both domains generally causes the effective bulk composition to decrease significantly in MnO, FeO and Y_2O_3 contents, and to increase in Na_2O, K_2O and TiO_2 contents, whereas all other element concentrations remain nearly constant. This is illustrated in Fig. 10, and by the results of the gain/loss calculations in Table 5. Figure 10a and b also shows that the effective bulk composition with respect to the major elements changes little during the first seven fractionation steps, but undergoes a significant change afterwards. The interval of rapidly changing composition correlates well with the significant increase of the garnet mode, as shown in Fig. 10e and f. In contrast to the major elements, the Y_2O_3 content decreases nearly linearly during garnet growth, indicating that Y_2O_3 was available during the whole garnet nucleation and growth evolution, but followed a different fractionation trend compared with MnO. From the evolution of the mode (Fig. 10e and f) it can be concluded that the linear decrease of the Y_2O_3 content in the rock volume was initially controlled by the formation of the Y-rich, flat-top garnet cores (steps 1–6), and subsequently (steps 6–12) by the formation of the Y-poor, but

more voluminous garnet overgrowths. It should be emphasized that the linear Y_2O_3 decrease, as shown in Fig. 10c and d, reflects the general fractionation trend in a rock volume of about 1 mm³, which contains *c.* 110 garnet grains (Table 1). In contrast to this linear trend, the Y zonation profiles of individual garnet grains show an abrupt change at the flat-top core–zoned overgrowth transition (Fig. 5l). It seems likely that this effect results from kinetic factors, e.g. from transport or interface kinetics, as discussed above.

Finally, it should be noted that the general form of the MnO fractionation curve in Fig. 10 is inconsistent with Rayleigh fractionation. In the case of Rayleigh fractionation, the whole-rock MnO content should decrease linearly (similar to the Y_2O_3 curves in Fig. 10).

FRACTIONATION-CORRECTED PHASE DIAGRAMS
General comments

To show the effect of garnet fractionation on the topology of quantitative phase diagrams, *P–T* pseudo-sections were constructed for the P- and B-domains. The first set of diagrams is constructed for the unfractionated bulk composition (Fig. 11a and c), and the second for the fractionated bulk composition reflecting the end of the garnet growth history (Fig. 11c and d). The calculations were carried out using the computer software THERMOCALC, version 3.1, with the internally consistent thermodynamic dataset HP98 (Holland & Powell, 1998), and *a–X* relationships as presented by White *et al.* (2001) and Zeh & Holness (2003). The calculations were carried out in the model system TiO_2–MnO–FeO–MgO–CaO–Na_2O–K_2O–Al_2O_3–SiO_2–H_2O (TiMnCNKFMASH), which is adequate to explain the minerals Grt, Bt, Chl, Ms, Pl, Qtz, Ilm and Ru observed in the investigated sample. H_2O was assumed to be in excess. This assumption is reasonable because carbonate was not observed in the investigated sample, and important amounts of H_2O must have been released during garnet growth as a result of chlorite breakdown. Y_2O_3 was neglected for several reasons. First, there are no any thermodynamic end-member data for Y-bearing minerals. Second, the amount of Y is very low in the investigated rock (*c.* 50 ppm). Third, Y is not available at the margins of the flat-top garnet cores, indicating that Y has no important influence on the thermodynamic stability of the garnet core composition, but is perhaps responsible for garnet nucleation and initial garnet growth (see above). Finally, the Y content is very low during the formation of the zoned garnet overgrowths (*c.* 200 ppm). Thus the composition of the flat-top garnet cores (at their Y-free margins) and of the zoned garnet overgrowths can be described by the model system

Table 5: *Gain and loss of elements (in mol %) in the effective bulk composition during 12 garnet growth steps*

	SiO_2	TiO_2	Al_2O_3	FeO	MgO	MnO	CaO	K_2O	Na_2O	H_2O	Y_2O_3
P-domain											
Step 1	65·5	1·18	12·1	5·4	2·4	1·87	4·17	0·46	5·5	1·40	1·36E – 03
Step 2	65·6	1·18	12·1	5·4	2·4	1·86	4·17	0·46	5·5	1·41	1·22E – 03
Step 3	65·6	1·19	12·1	5·4	2·4	1·84	4·17	0·47	5·5	1·41	9·55E – 04
Step 4	65·6	1·19	12·1	5·4	2·4	1·80	4·16	0·47	5·5	1·41	6·22E – 04
Step 5	65·7	1·19	12·1	5·3	2·4	1·76	4·16	0·47	5·5	1·41	3·28E – 04
Step 6	65·8	1·20	12·1	5·2	2·4	1·69	4·15	0·47	5·5	1·42	1·32E – 04
Step 7	66·0	1·21	12·1	5·1	2·4	1·58	4·14	0·47	5·6	1·43	3·60E – 05
Step 8	66·4	1·23	12·1	4·8	2·4	1·40	4·11	0·48	5·7	1·46	5·19E – 06
Step 9	67·2	1·27	12·0	4·2	2·4	1·04	4·06	0·50	5·9	1·51	1·88E – 07
Step 10	68·4	1·33	11·9	3·3	2·3	0·61	4·00	0·52	6·1	1·58	2·77E – 19
Step 11	69·7	1·40	11·7	2·1	2·2	0·15	3·92	0·55	6·5	1·66	2·92E – 19
Step 12	70·1	1·42	11·7	1·8	2·2	0·06	3·91	0·56	6·5	1·69	2·95E – 19
Gain/loss(%)	7	20	–4	–66	–6	–97	–6	20	20	20	–100
B-domain											
Step 1	66·7	0·57	8·5	7·4	5·4	1·70	2·42	1·50	2·4	3·4	9·77E – 04
Step 2	66·7	0·57	8·5	7·4	5·4	1·69	2·41	1·51	2·4	3·4	8·15E – 04
Step 3	66·7	0·57	8·5	7·4	5·4	1·66	2·41	1·51	2·4	3·4	6·10E – 04
Step 4	66·8	0·57	8·5	7·3	5·4	1·63	2·40	1·51	2·4	3·5	3·93E – 04
Step 5	66·9	0·57	8·5	7·3	5·4	1·59	2·39	1·52	2·4	3·5	2·09E – 04
Step 6	67·0	0·57	8·4	7·2	5·5	1·53	2·38	1·52	2·4	3·5	8·63E – 05
Step 7	67·2	0·58	8·4	7·1	5·5	1·43	2·35	1·54	2·4	3·5	2·47E – 05
Step 8	67·5	0·59	8·3	6·9	5·5	1·26	2·30	1·56	2·4	3·6	3·85E – 06
Step 9	68·4	0·61	8·1	6·4	5·6	0·92	2·19	1·61	2·5	3·7	1·62E – 07
Step 10	69·5	0·63	7·8	5·6	5·7	0·52	2·05	1·68	2·6	3·8	1·54E – 20
Step 11	70·7	0·66	7·5	4·7	5·8	0·12	1·90	1·76	2·8	4·0	1·61E – 20
Step 12	70·7	0·66	7·5	4·7	5·8	0·12	1·90	1·76	2·8	4·0	1·61E – 20
Gain/loss(%)	6	17	–11	–37	8	–93	–22	17	17	17	–100

TiMnCNKFMASH. To show the agreement between measured and calculated garnet compositions, all diagrams in Fig. 11 were contoured for X_{sps}. In addition, some relevant contours for X_{grs} and X_{alm} are shown as well.
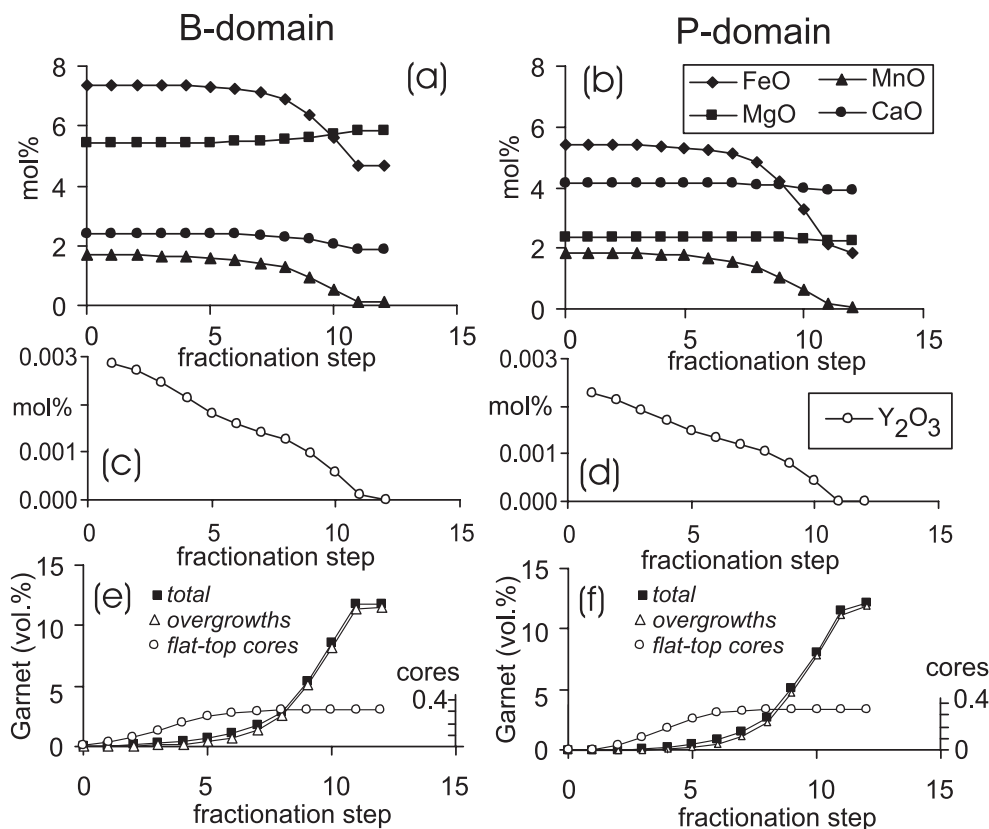
Results

The phase diagrams constructed without fractionation (Fig. 11a and c) provide evidence that the core of the largest garnet grain of the P-domain was formed at *P–T* conditions of *c*. 470°C at 2·7 kbar in the assemblage Ms–Bt–Chl–Grt–Pl–Ilm–Qtz–H_2O, whereas the core of the largest garnet grain of the B-domain was formed in the same assemblage but at somewhat higher *P–T* conditions of *c*. 485°C at 3·3 kbar (Table 6). These *P–T* conditions are constrained by the agreement between the observed and calculated mineral assemblages and garnet compositions. As shown in Fig. 11a and c,

the calculated X_{sps}, X_{alm} and X_{grs} isopleths, which correspond to the measured garnet core compositions of the largest garnet grains (P221, B339), intersect at one point within the assemblage observed in the thin section.

However, the two phase diagrams calculated without garnet fractionation (Fig. 11a and c) are of only limited use in explaining the complete garnet growth zonation of the grains P221 and B339, in particular their rim compositions (Table 6), as well as the core compositions of essentially smaller garnet grains (e.g. grain B125). The rim compositions can be predicted only when the effect of garnet fractionation is taken into account (Fig. 11b and d). The agreement between the measured and calculated garnet rim compositions indicates that garnet growth at fractionation step 12 (MnO^{Grt} = 8·1 mol %) occurred at *P–T* conditions of about 570°C at 7·3 kbar, and that the most evolved garnet rim (MnO^{Grt} = 5·6 mol %) grew at *P–T* conditions of about 580°C at 8·4 kbar (Table 6). Identical *P–T* conditions are also

Fig. 10. Results of fractionation calculations. (a–d) Bulk composition (mol %) vs fractionation step diagrams, showing the change of the effective bulk composition during successive garnet growth with respect to FeO, MnO, MgO and CaO (a, b) and Y_2O_3 (c, d) in the B- and P-domains. (e, f) Garnet mode (vol. %) vs fractionation step diagram, showing the change of the garnet volume (total, flat-top core and overgrowths) during successive garnet growth. During the first six fractionation steps most of the flat-top garnet core volume is formed (c. 0·3–0·4 vol. %), whereas the garnet overgrowth volume increases significantly from step 7 to step 12. (For further explanation see text.)

obtained by conventional geothermobarometry (Table 7) using the 'average P–T conditions' feature of THERMOCALC in conjunction with the program A-x (T. Holland, personal communication, 2005), and mineral compositions as shown in Tables 2 and 3.

The results shown in Fig. 11 indicate that garnet fractionation has several effects on the phase diagram topology, e.g. the stability of garnet and ilmenite is reduced toward higher P and/or T conditions, whereas the stability field of rutile increases toward lower pressures (because of loss of MnO and FeO, and gain of TiO_2 and MgO). In addition, the upper temperature stability limit of muscovite and chlorite is enlarged (MgO, K_2O and Na_2O gain). Garnet fractionation also causes the X_{sps} isopleths to become condensed towards lower P–T conditions compared with those in the 'unfractionated' diagrams (Fig. 11). In contrast, the X_{grs} isopleths remain nearly stationary, and the X_{alm} isopleths shift only slightly to higher temperatures or rotate slightly within the assemblage Ms–Bt–Chl–Grt–Pl–Ru–Qtz–H_2O. In general, the shift of the isopleths as a result

of garnet fractionation has only a slight effect on the inferred P–T vector. As shown in Figs 11 and 12, P–T vectors inferred either with or without considering garnet fractionation are nearly identical and both require a P–T increase during garnet growth.

The P–T vector in the 'unfractionated' diagrams is best constrained along the X_{grs} = 13 isopleths and accounts for the occurrence of ilmenite inclusions in garnet and of matrix rutile in assemblage with Ms–Bt–Chl–Grt–Pl–Qtz–H_2O. In addition, it explains the observed decrease of X_{sps} and increase of X_{alm} from garnet core to rim, although the absolute spessartine content at the calculated garnet rim is too high and the almandine content too low. In contrast, the P–T vector obtained by considering fractionation explains not only the observed change of the mineral assemblage during garnet formation, but also the absolute garnet composition throughout the entire garnet growth evolution (Fig. 12, Table 6).

Table 6 and Fig. 12 present the P–T results obtained by garnet isopleth geothermobarometry for the
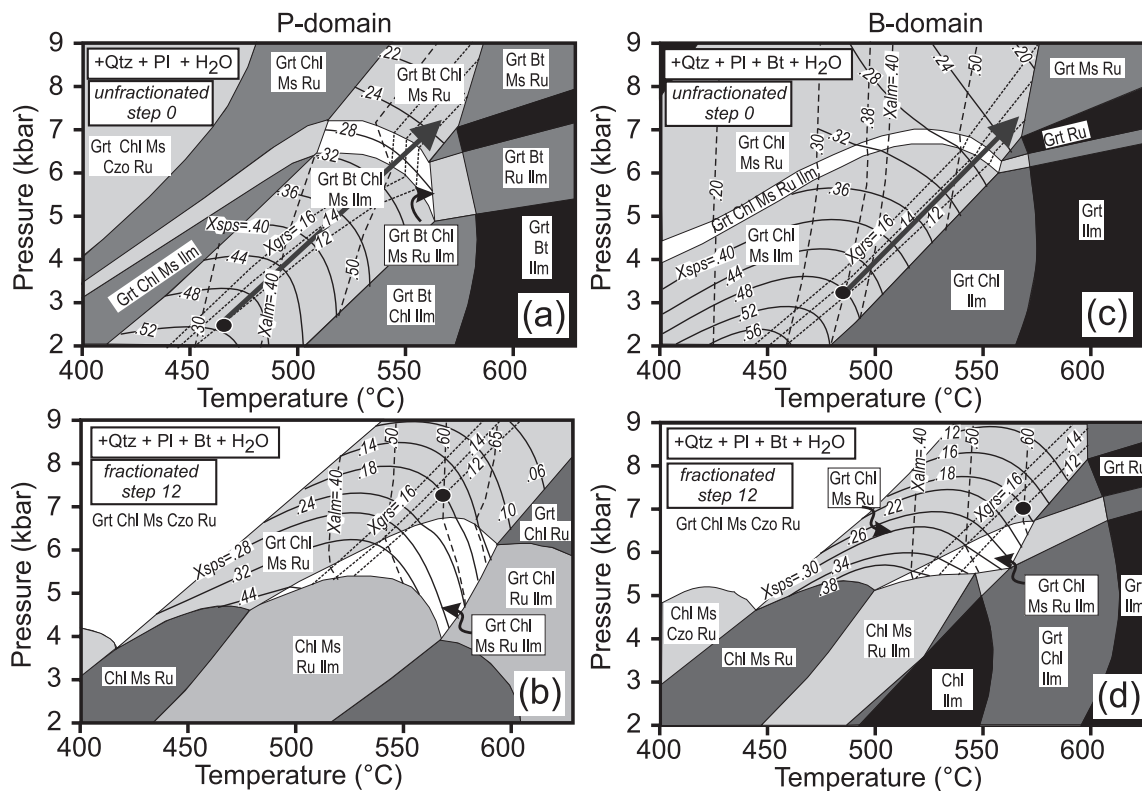
Fig. 11. P–T pseudosections calculated with THERMOCALC for the P-domain (a, b) and B-domain (c, d). The diagrams in (a) and (c) are calculated without garnet fractionation, and the diagrams in (b) and (d) with fractionation, using the effective bulk compositions as shown in Table 5. The black circles indicate the P–T conditions at which the measured and calculated garnet compositions fit (see Table 6). The black arrows in (a) and (c) show the P–T vectors, which best explain the observed assemblages and garnet zonation patterns if garnet fractionation is not considered. (For further explanation see text.)

fractionation steps 0, 3, 6, 9 and 12. In addition, they show the MnO content at garnet rims at the respective garnet growth step and the corresponding garnet mode (in vol. %). The P–T results indicate that the investigated garnet population was formed during a linear P–T increase from 470°C and 2·7 kbar to 580°C and 8·4 kbar. The results also demonstrate that during the first pressure increase of c. 2·5 kbar only 1 vol. % garnet was formed (steps 0–6), but that 10–11 vol. % garnet grew during the subsequent pressure increase of further 2·5 kbar (steps 6–12).

The P–T results, in combination with the mineral chemical data, also indicate that the flat-top garnet cores, which all have high Y_2O_3 contents of c. 1 wt % (Table 2, Figs 5 and 8h), nucleated and grew over a temperature interval of about 90°C [from 470°C and 2·7 kbar (MnO 22·5 wt %) to 560°C and 7 kbar (MnO 10 wt %)]. This result is of particular significance, because it shows that the Y content of the garnet cores is relatively insensitive to temperature change. This result is different from that of Pyle & Spear (2000). Those researchers postulated that the Y content of garnet decreases logarithmically during a temperature increase

from 450 to 600°C, provided that garnet is formed in an assemblage that contains xenotime. In contrast to Pyle & Spear's (2000) study, xenotime was not found in the investigated sample, which contains only accessory allanite, apatite, zircon, ilmenite and rutile.

SUMMARY AND CONCLUSIONS
In this study the effect of garnet fractionation was calculated using textural and compositional parameters obtained from both a plagioclase-rich and a biotite-rich domain of a garnet–biotite gneiss sample from the Ruhla Crystalline Complex. The calculation incorporated consideration of the mode and composition of all unzoned minerals, as well as the mode, CSD, and zonation patterns of garnet grains of different sizes within a certain rock volume.

The investigated garnet grains show typical flat-top geometries with respect to MnO, and the garnet MnO evolution reflects a time line. Away from the unzoned garnet cores, which perhaps result from fast kinetically controlled garnet growth, all zoned garnet overgrowths

Table 6: Comparison between measured and calculated garnet compositions during fractionated garnet growth

Step*	Assem.†	MnO in Grt (wt %)	Grt (vol. %) calc.	T (°C)	P (kbar)	X_{grs} meas.	X_{grs} calc.	X_{sps} meas.	X_{sps} calc.	X_{alm} meas.	X_{alm} calc.
P-domain											
1	ilm	22·5	0·005	469	2·7	0·12	0·12 (0·01)	0·51	0·51 (0·02)	0·36	0·35 (0·03)
3	ilm	19·8	0·14	490	3·8	0·13	0·13 (0·01)	0·45	0·44 (0·02)	0·40	0·40 (0·03)
6	ilm	15·9	0·89	520	5·1	0·13	0·13 (0·01)	0·36	0·36 (0·02)	0·47	0·47 (0·02)
9	ru + ilm	12·0	5·1	551	6·6	0·13	0·13 (0·01)	0·27	0·26 (0·02)	0·54	0·53 (0·02)
12	ru	8·1	12·2	570	7·3	0·12	0·12 (0·01)	0·18	0·18 (0·02)	0·60	0·60 (0·03)
	ru	5·6		577	8·4	0·16	0·16 (0·01)	0·13	0·12 (0·02)	0·63	0·62 (0·02)
B-domain											
1	ilm	21·1	0·03	486	3·3	0·13	0·13 (0·01)	0·48	0·48 (0·02)	0·38	0·37 (0·02)
3	ilm	18·8	0·22	505	4·1	0·13	0·13 (0·01)	0·42	0·42 (0·02)	0·42	0·42 (0·02)
6	ilm	15·3	0·98	527	5·2	0·13	0·13 (0·01)	0·34	0·34 (0·02)	0·48	0·48 (0·02)
9	ru + ilm	11·8	5·2	547	6·2	0·13	0·13 (0·01)	0·27	0·26 (0·02)	0·54	0·54 (0·02)
12	ru	8·3	11·3	566	7·1	0·13	0·13 (0·01)	0·19	0·19 (0·02)	0·60	0·59 (0·03)
	ru	5·6		575	8·1	0·16	0·16 (0·01)	0·13	0·12 (0·02)	0·63	0·62 (0·02)

*Fractionation step.
†Assemblage, all with grt, bt, chl, ms, pl, qtz, H_2O.
meas., Grt composition measured; calc., Grt composition calculated with THERMOCALC; values in parentheses are error of calculations.

Table 7: Results of P–T calculations using mineral rim compositions

	T (°C)	S.D.	P (kbar)	S.D.	Corr.	Sigfit
B178	580	21	8·0	1·1	0·509	1·46
P221	570	20	7·7	1·1	0·515	1·38
B125	568	20	7·7	1·1	0·520	1·37
P388	587	21	8·1	1·1	0·531	1·46
B339	572	21	8·2	1·1	0·520	1·44

All calculations were carried out for X_{H_2O} = 1.0; S.D., 2σ standard deviation; corr. and sigfit. obtained with THERMOCALC. Mineral end-members used for calculations are: py, gr, alm, mu, pa, cel, phl, ann, east, clin, daph, ames, an, ab, q, H_2O [abbreviations according to Holland & Powell (1998)]. (For further explanation see the text.)

grew with nearly the same radial growth rate at each stage of the garnet growth evolution. Eight functions, (F1)–(F8), are necessary to calculate the amount of garnet fractionation at each step of the garnet growth history.

The results of fractionation calculations indicate that MnO, FeO and Y_2O_3 are extremely fractionated during garnet growth, but in different ways. MnO and FeO concentrations remained nearly unchanged at the beginning of the garnet growth evolution (step 1–6) and then underwent a significant change (steps 6–12). In contrast, the Y_2O_3 concentration decreased nearly linearly throughout garnet growth in the considered rock

volumes. The MnO garnet zonation patterns provide evidence that the MnO content in the investigated rock is not obeying a Rayleigh fractionation trend. This is evident from the finding that the garnet porphyroblasts do not show typical bell-shaped zonation patterns, and that the MnO content of the effective bulk composition does not decrease linearly with the garnet's MnO content. This indicates that garnet fractionation calculations using a Rayleigh fractionation model may yield imprecise results. If a Rayleigh fractionation model is used (e.g. Evans, 2004) it should first be determined whether or not the garnet grains in the investigated rock show bell-shaped zonation patterns that can be fitted by
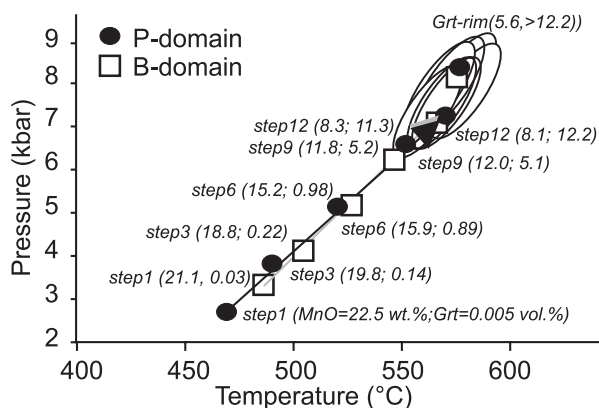
Fig. 12. P–T diagram showing the P–T points inferred from the agreement between measured and calculated garnet compositions and mineral assemblages in the P- and B-domains (see Table 6). For each fractionation step the MnO content of garnet (in wt %), and the garnet mode (in vol. %) is additionally shown. The ellipses represent results of conventional geothermobarometry. The arrows show the P–T vectors obtained without garnet fractionation for the P-domain (black) and B-domain (grey), as shown in Fig. 11. (For further explanation see text.)

a Rayleigh function using a certain fractionation coefficient (e.g. Hollister, 1966).

Quantitative phase diagrams constructed in the model system Na_2O–K_2O–CaO–MnO–FeO–MgO–Al_2O_3–TiO_2–SiO_2–H_2O indicate that complete garnet growth zonation profiles can be accurately predicted when the effect of successive bulk-rock modification as a result of garnet fractionation is taken into account. The diagrams also show that identical P–T vectors will be obtained, independent of whether the phase diagrams were calculated with or without fractionation. Comparison between calculated and measured garnet compositions (garnet isopleth geothermobarometry) indicates that garnet growth in the investigated metapelite occurred along a linear P–T path from 470°C and 2·7 kbar to 580°C and 8·5 kbar.

The combined results of textural and compositional analyses with P–T path estimates indicate that garnet cores with high Y_2O_3 contents of about 1 wt % were formed over a temperature interval of c. 90°C. This shows that the Y content in garnet is relatively insensitive to temperature, and perhaps controlled by kinetic rather than by thermodynamic parameters.

ACKNOWLEDGEMENTS

REFERENCES

Carlson, W. D. (1989). The significance of intergranular diffusion to the mechanisms and kinetics of porphyroblast crystallization. *Contributions to Mineralogy and Petrology* **103**, 1–24.

Chernoff, C. B. & Carlson, W. D. (1997). Disequilibrium for Ca during growth of pelitic garnet. *Journal of Metamorphic Geology* **15**, 421–438.

Daniel, C. G. & Spear, F. S. (1999). The clustered nucleation and growth processes of garnet in regional metamorphic rocks from north-west Connecticut, USA. *Journal of Metamorphic Geology* **17**, 503–520.

De Capitani, C. & Brown, T. H. (1986). The computation of chemical equilibrium in complex systems containing non-ideal solutions. *Geochimica et Cosmochimica Acta* **51**, 2639–2652.

Evans, T. P. (2004). A method for calculating effective bulk composition modification due to crystal fractionation in garnet-bearing schist: implications for isopleth thermobarometry. *Journal of Metamorphic Geology* **22**, 547–557.

Florence, F. P. & Spear, F. S. (1991). Effects of diffusional modification of garnet growth zoning on P–T path calculations. *Contributions to Mineralogy and Petrology* **107**, 487–500.

Hauzenberger, C. A., Robl, J. & Stüwe, K. (2005). Garnet zoning in high-pressure granulite-facies metapelites, Mozambique belt, SE Kenya: constraints on the cooling history. *European Journal of Mineralogy* **17**, 43–55.

Hickmott, D. D. & Shimizu, N. (1990). Trace element zoning in garnet from the Kwoiek Area, British Columbia: disequilibrium partitioning during garnet growth? *Contributions to Mineralogy and Petrology* **104**, 619–630.

Hirsch, D. M., Prior, D. J. & Carlson, W. D. (2003). An overgrowth model to explain multiple, dispersed high-Mn regions in the cores of garnet porphyroblasts. *American Mineralogist* **88**, 131–141.

Holland, T. J. B. & Powell, R. (1998). An internally consistent thermodynamic data set for phases of petrological interest. *Journal of Metamorphic Geology* **16**, 309–343.

Hollister, L. S. (1966). Garnet zoning: an interpretation based on the Rayleigh fractionation model. *Science* **154**, 1647–1651.

Konrad-Schmolke, M., Handy, M. R., Babist, J. & O'Brien, P. J. (2005). Thermodynamic modelling of diffusion-controlled garnet growth. *Contributions to Mineralogy and Petrology* **149**, 181–195.

Kretz, R. (1966). Grain size distribution for certain metamorphic minerals in relation to nucleation and growth. *Journal of Geology* **74**, 147–173.

Kretz, R. (1974). Some models for the rate of crystallization of garnet in metamorphic rocks. *Lithos* **7**, 123–131.

Lanzirotti, A. (1995). Yttrium zoning in metamorphic garnets. *Geochimica et Cosmochimica Acta* **59**, 4105–4110.

Marmo, B. A., Clarke, G. L. & Powell, R. (2002). Fractionation of bulk rock composition due to porphyroblast growth; effects on eclogite facies mineral equilibria, Pam Penninsula, New Caledonia. *Journal of Metamorphic Geology* **20**, 151–165.

Meth, C. E. & Carlson, W. D. (2005). Diffusion controlled synkinematic growth of garnet from a heterogeneous precursor at Passo del Sol, Switzerland. *Canadian Mineralogist* **43**, 157–182.

Milke, R. & Metz, P. (2002). Experimental investigation of the kinetics of the reaction wollastonite + calcite + anorthite = grossular + CO_2. *American Journal of Science* **302**, 312–345.

Powell, R., Holland, T. J. B. & Worley, B. (1998). Calculating phase diagrams involving solid solutions via non-linear equations, with

examples using THERMOCALC. *Journal of Metamorphic Geology* **16**, 577–588.

Pyle, J. M. & Spear, F. S. (2000). An empirical garnet (YAG)–xenotime thermometer. *Contributions to Mineralogy and Petrology* **138**, 51–58.

Spear, F. S. (1993). *Metamorphic Phase Equilibria and Pressure–Temperature–Time Paths.* Washington, DC: Mineralogical Society of America, pp. 799.

Spear, F. S., Kohn, M. J., Florence, F. P. & Menard, T. (1990). A model for garnet and plagioclase growth in pelitic schists; implications for thermobarometry and *P–T* path determinations. *Journal of Metamorphic Geology* **8**, 683–696.

Stüwe, K. (1997). Effective bulk composition change due to cooling: a model predicting complexities in retrograde reaction textures. *Contributions to Mineralogy and Petrology* **129**, 43–52.

Vance, D. & Mahar, E. (1998). Pressure–temperature paths from *P–T* pseudosections and zoned garnets; potential, limitations and examples from the Zanskar Himalaya, NW India. *Contributions to Mineralogy and Petrology* **132**, 225–245.

Watson, E. B. (1996). Surface enrichment and trace-element uptake during crystal growth. *Geochimica et Cosmochimica Acta* **60**, 5013–5020.

White, R. W., Powell, R., Holland, T. J. B. & Worley, B. A. (2000). The effect of TiO_2 and Fe_2O_3 on metapelitic assemblages at greenschist and amphibolite facies conditions: mineral equilibria calculations in the system K_2O–FeO–MgO–Al_2O_3–SiO_2–H_2O–TiO_2–Fe_2O_3. *Journal of Metamorphic Geology* **18**, 497–511.

White, R. W., Powell, R. & Holland, T. J. B. (2001). Calculation of partial melting equilibria in the system Na_2O–CaO–K_2O–FeO–MgO–Al_2O_3–SiO_2–H_2O (NCKFMASH). *Journal of Metamorphic Geology* **19**, 139–153.

Zeh, A. (1996). Die Druck–Temperatur–Deformations-Entwicklung des Ruhlaer Kristallins. *Geotektonische Forschungen* **86**, 212 S.

Zeh, A. (2001). Inference of a detailed *P–T* path from *P–T* pseudosections using metapelitic rocks of variable composition from a single outcrop, Shackleton Range, Antarctica. *Journal of Metamorphic Geology* **19**, 329–350.

Zeh, A. & Holness, M. (2003). The effect of reaction overstep on garnet microtextures in metapelitic rocks of the Ilesha Schist Belt, SW Nigeria. *Journal of Petrology* **44**, 967–994.

Zeh, A. & Millar, I.L. (2001). Metamorphic evolution of garnet–epidote–biotite gneiss from the Moine Supergroup, Scotland, and geotectonic implications. *Journal of Petrology* **42**, 529–554.

APPENDIX A: METHODS
Crystal size distribution (CSD) analysis of garnet

Garnet grains were counted and measured in certain volumes of the P-domain (15·5 mm^3) and B-domain (11·3 mm^3) using a thick section of originally 518 µm thickness, and four grinding steps at 405, 300, 203 and 98 µm. The thickness tolerance of each grinding step was *c.* 3 µm, as checked with a microscrew on several edges of the thick section after each grinding step. Prior to grinding, the boundaries of the investigated P- and B-domains were marked with a laser, used to drill holes of *c.* 30 µm diameter though the entire thick section.

The *c.* 100 µm spacing of the grinding steps is suitable for detecting all garnet grains with sizes between 20 and 255 µm, even in biotite-rich and, thus, less transparent domains. Prior to the garnet grain-size measurements, the investigated areas of the P- and B-domains were systematically photographed with a digital camera with a magnification of *c.* 200× for each grinding step in transmitted and reflected light. Subsequently, these photographs, in combination with direct microscopic observations in transmitted light, were used to document the position of each garnet grain. Finally, the maximum diameter of each garnet grain was directly measured in the thick section using the ocular microscale of a Leica microscope, calibrated against a Leica object micrometer. With this procedure it is possible to measure the true diameter of each garnet grain with an accuracy of ±3 µm.

Point counting

The mineral modes of the P- and B-domains (see Table 1) were analysed by point counting using a SWIFT point counter with grid space of *c.* 0·25 mm × 0·25 mm. Point counting was carried out on the thin section, which remained after final ginding of the thick section to a thickness of 30 µm. The CSD measurements and mode analyses were carried out on exactly the same domains.

Microprobe analysis, sample preparation, and XRF analysis

Electron microprobe analyses were carried out with a CAMECA SX-50 microprobe at the Mineralogical Institute, University of Würzburg, and with a JEOL microprobe at the University of Frankfurt (Department of Mineralogy). The CAMECA SX-50 microprobe is equipped with three independent wavelength-dispersive crystal channels. Instrument conditions were 15 kV acceleration voltage, 15 nA specimen current, and 20 s integration time for all elements except for Fe (30 s). Natural and synthetic silicates and oxides were used for reference, and matrix corrections were carried out using the PAP program supplied by CAMECA. Point analyses were performed with a 10 µm beam diameter for muscovite, and a 1 µm beam diameter for all other minerals. Lower limits of detection (1σ) for a typical silicate analysis were ∼1 wt % relative for each element. Qualitative element maps of garnet were made with the JEOL microprobe using instrument conditions of 15 kV acceleration voltage, 3 nA specimen current, and 400 ms dwell time for all elements. The zonation profiles and qualitative element maps were measured on centrally cut garnet grains. These grains were carefully selected according to the following criteria. In a first step the maximum diameters of all garnet grains below the thick-section surface (0–150 µm)

were measured in transmitted light (see above). Second, after grinding ($c.$ 100 μm) the new surface of the thick section was investigated under reflected light. Centrally cut garnet grains are those that yielded the same diameter during both measurements. Third, from these centrally cut garnet grains I selected grains of different sizes, in particular those that exposed six edges at the thick-section surface (see Fig. 5).

Bulk compositions were analysed by conventional XRF spectrometry using a Phillips PW 1480 spectrometer (University of Würzburg), and lithium tetraborate fusion discs, and the loss on ignition method.

LA–ICP–MS analysis

Laser ablation–inductively coupled plasma–mass spectrometry (LA-ICP-MS) garnet measurements were carried out at the Mineralogical Institute, University of Würzburg, using a Merchantek LUV 266 nm laser coupled with a quadrupole AGILENT 7500i ICP-MS system. For quantitative analyses carefully selected garnet grains were drilled with the laser for $c.$ 30 s using a laser spot size of $c.$ 30 μm, $c.$ 0·25 mJ energy and a repetition rate of $c.$ 10 Hz. Time-resolved signals were compared with the glass reference material standards NIST SRM 612 and SRM 614, using SiO_2 ($c.$ 36 wt %) as the internal standard. The measured signal was quantified with the software GLITTER 3·0.

APPENDIX B: CALCULATION OF THE NUMBER OF MOLES OF ALL UNZONED PHASES

The moles of each phase (M^k) were calculated using the equations (5) and (6). The volumes of all unzoned minerals (V^k) and their chemical compositions were determined by point counting (Table 1) and electron microprobe analysis (Table 3, average compositions). From the measured mineral composition the mole fractions of the phase components j (e.g. X_{an}^{Pl}, X_{ab}^{Pl}, X_{pa}^{Ms}, etc.) were estimated as follows.

Plagioclase (X^{Pl}) $Na_{1-x}Ca_xAl_{1+x}Si_{3-x}O_8$

$X_{an} = Ca/(Ca + Na)$

$X_{ab} = Na/(Ca + Na)$

Biotite (X^{Bt}) $K^A(Fe,Mg,Mn,Ti,Al,vac)_3^{VI}(Al,Si)_2^{IV}Si_2O_{10}(OH)_2$

Annite: $K(Fe)_3^{VI}AlSi_3O_{10}(OH)_2$; $X_{ann} = x_{ann}/\mathcal{N}$
Mn-biotite: $K(Mn)_3^{VI}AlSi_3O_{10}(OH)_2$; $X_{MnBt} = x_{MnBt}/\mathcal{N}$
Eastonite: $K(Mg_2,Al)^{VI}Al_2Si_2O_{10}(OH)_2$; $X_{east} = x_{east}/\mathcal{N}$
Ti-biotite: $K(MgTi,vac)^{VI}AlSi_2O_{10}(OH)_2$; $X_{TiBt} = x_{TiBt}/\mathcal{N}$
Phlogopite: $K(Mg)_3^{VI}AlSi_3O_{10}(OH)_2$; $X_{phl} = x_{phl}/\mathcal{N}$
Talc: $(Mg)_3^{VI}Si_4O_{10}(OH)_2$; $X_{talc} = x_{talc}/\mathcal{N}$

$x_{ann} = Fe^{VI}/3$
$x_{MnBt} = Mn^{VI}/3$
$x_{TiBt} = Ti^{VI}$
$x_{east} = Al^{VI}$
$x_{phl} = Al^{IV} - x_{TiBt} - 2x_{east} - x_{MnBt} - x_{ann}$
$x_{talc} = (Mg^{VI} - x_{TiBt} - 2x_{east} - 3x_{phl})/3$
$\mathcal{N} = x_{ann} + x_{MnBt} + x_{east} + x_{TiBt} + x_{phl} + x_{talc}$

Muscovite (X^{Ms}) $(K,Na)^A(Fe,Mg,Al)_2^{VI}(Al,Si)Si_3O_{10}(OH)_2$

Paragonite: $Na^A(Al)_2^{VI}AlSi_3O_{10}(OH)_2$; $X_{pa} = x_{pa}/\mathcal{N}$
Fe-Celadonite: $K^A(Fe,Al)^{VI}Si_4O_{10}(OH)_2$; $X_{fecel} = x_{fecel}/\mathcal{N}$
Celadonite: $K^A(MgAl)^{VI}Si_4O_{10}(OH)_2$; $X_{cel} = x_{cel}/\mathcal{N}$
Muscovite: $K^A(Al)_2^{VI}AlSi_3O_{10}(OH)_2$; $X_{ms} = x_{ms}/\mathcal{N}$

$x_{pa} = Na^A$
$x_{fecel} = Fe^{VI}$
$x_{cel} = Mg^{VI}$
$x_{ms} = (K^A - X_{fecel} - X_{cel})/3$
$\mathcal{N} = x_{pa} + x_{ms} + x_{fecel} + x_{cel}$

Chlorite (X^{Chl}) $(Fe,Mg,Mn,Al)_6^{VI}(Al,Si)_2^{IV}Si_2O_{10}(OH)_8$

Amesite: $Mg_4Al_2Al_2Si_2O_{10}(OH)_8$; $X_{ames} = x_{ames}/\mathcal{N}$
Mn-Chlorite: $Mn_5AlAlSi_3O_{10}(OH)_8$; $X_{MnChl} = x_{MnChl}/\mathcal{N}$
Clinochlore: $Mg_5AlAlSi_3O_{10}(OH)_8$; $X_{clin} = x_{clin}/\mathcal{N}$
Daphnite: $Fe_5AlAlSi_3O_{10}(OH)_8$; $X_{daph} = x_{daph}/\mathcal{N}$

$x_{ames} = Al^{VI} - 1$
$x_{MnChl} = 1/5 \times Mn^{VI}$
$x_{daph} = 1/5 \times Fe^{VI}$
$x_{clin} = 1/5 \times (Mg^{VI} - 4\ ames)$
$\mathcal{N} = x_{ames} + x_{MnChl} + x_{clin} + x_{daph}.$

The molar volumes of the considered phase components (v_j) were obtained from the thermodynamic dataset of Holland & Powell (1998) at standard state conditions.